

See discussions, stats, and author profiles for this publication at: <https://www.researchgate.net/publication/243971622>

Adsorption of α,β -Unsaturated Aldehydes on Pt(111) and Pt–Sn Alloys: II. Crotonaldehyde

ARTICLE in THE JOURNAL OF PHYSICAL CHEMISTRY C · AUGUST 2009

Impact Factor: 4.77 · DOI: 10.1021/jp903473m

CITATIONS

23

READS

35

7 AUTHORS, INCLUDING:



Jan Haubrich

German Aerospace Center (DLR)

38 PUBLICATIONS 624 CITATIONS

SEE PROFILE



Aleksander Ryszard Krupski

University of Portsmouth

52 PUBLICATIONS 349 CITATIONS

SEE PROFILE



C. Becker

Aix-Marseille Université

91 PUBLICATIONS 1,411 CITATIONS

SEE PROFILE



Klaus Rainer Wandelt

University of Bonn

436 PUBLICATIONS 8,076 CITATIONS

SEE PROFILE

Adsorption of α,β -Unsaturated Aldehydes on Pt(111) and Pt–Sn Alloys: II. CrotonaldehydeJ. Haubrich,^{*,†} D. Loffreda,[‡] F. Delbecq,[‡] P. Sautet,[‡] A. Krupski,[§] C. Becker,[†] and K. Wandelt[†]

Institut für Physikalische und Theoretische Chemie, Universität Bonn, Wegelerstrasse 12, D-53115 Bonn, Germany, Université de Lyon, Institut de Chimie de Lyon, Laboratoire de Chimie, Ecole Normale Supérieure de Lyon, CNRS, 46 Allée d'Italie, F-69364 Lyon Cedex 07, France, and Institute of Experimental Physics, University of Wrocław, pl. Maxa Borna 9, PL 50-204 Wrocław, Poland

Received: April 15, 2009; Revised Manuscript Received: June 7, 2009

By employing high-resolution electron energy loss spectroscopy (HREELS), temperature-programmed desorption (TPD), and low-energy electron diffraction (LEED), we have studied the adsorption and thermal decomposition of crotonaldehyde (2-butenal) on Pt(111) as well as Pt₃Sn/Pt(111) and Pt₂Sn/Pt(111) surface alloys. In order to understand the adsorption structures and the vibrational properties, an extensive theoretical study of the possible adsorption geometries and vibrational spectra on the three considered surfaces has been carried out using density functional theory (DFT). A careful analysis of the variety of possible adsorption configurations of crotonaldehyde allowed structural identification by correlating their vibrational fingerprints with the measured HREELS peaks. The mixed phases of crotonaldehyde formed on the model catalysts turned out to be even more complex than those we found in previous studies for prenal. The set of stable configurations identified by combination of HREELS with DFT consists of η^2 , η^3 , and η^4 flat adsorption structures, which exhibit adsorption energies from –69 to –80 kJ/mol. Nonetheless, the thermal decomposition measured with TPD and the general adsorption behavior show similarities to prenal and acrolein. Starting from a strongly adsorbed state on Pt(111) at low temperatures, crotonaldehyde decomposes at temperatures close to 300 K. On the surface alloys, a high-coverage phase with structures of low hapticity such as η^2 -di σ (CC) is measured at low temperatures (~160 K), and a low-coverage situation of high hapticity η^2 , η^3 , and η^4 configurations is formed at higher temperatures (~200 K). On Pt₃Sn/Pt(111), two energetically competitive η^1 -top-E-(s)-trans-OSn forms cannot be excluded at low temperatures.

1. Introduction

The selective hydrogenation of α,β -unsaturated aldehydes such as acrolein, crotonaldehyde (2-butenal), or prenal (3-methyl-2-buten-1-al) to α,β -unsaturated alcohols is a premier example of a complex catalytic process. The selectivity of the hydrogenation on poor catalysts generally leads to the thermodynamically favored saturated aldehydes or even alkanes, whereas improved catalysts shift the selectivity to the α,β -unsaturated alcohols,^{1,2} which are important fine chemicals in the fields of pharmacology, perfumes, and flavors.^{3–5} Much attention has been paid to the use of group VIII transition metals, including especially platinum as catalysts (see refs 6 and 7 and refs therein). However, their intrinsic selectivity and reactivity can be enhanced further by alloying with electropositive elements such as Sn, Fe, or Co.^{8–12}

For obtaining systematic insights into this catalytic mechanism and the reasons for improved selectivities, model catalyst studies of the interaction and thermal behavior of the reactants can be invaluable. Useful surface models of such a heterogeneous catalyst, which are accessible to surface sensitive experimental methods in ultrahigh vacuum, are the bimetallic Pt₃Sn/Pt(111) and Pt₂Sn/Pt(111) surface alloys (Figure 1). They can be prepared by physical vapor deposition of Sn on a Pt(111) single crystal and subsequent annealing.^{2,9,13–22} Around 700 K, the more tin-rich Pt₂Sn/Pt(111) monolayer alloy film is obtained

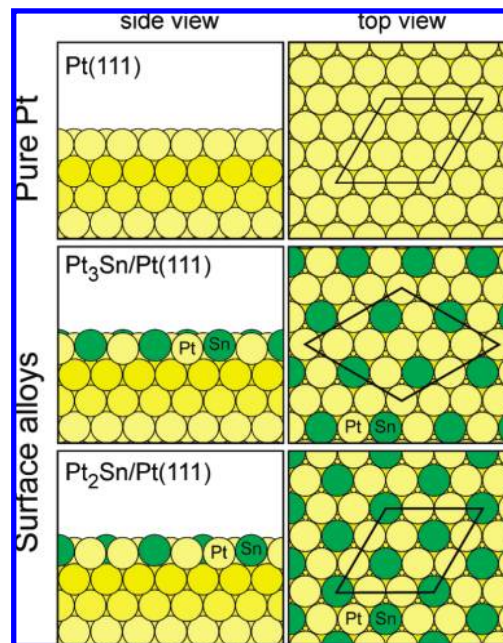


Figure 1. Schematic view of the (a) bare Pt(111) and the surface alloys (b) Pt₂Sn(111)/Pt(111) and (c) Pt₃Sn(111)/Pt(111). For each surface, the corresponding (3 × 3), (2 × 3), and (3 × 3) supercells used for the DFT calculations are indicated in the top views.

* To whom correspondence should be addressed. E-mail: janh@pc.uni-bonn.de. Fax: +49 228 73 2515.

[†] Universität Bonn.

[‡] Université de Lyon.

[§] University of Wrocław.

($\Theta_{\text{Sn}} = 0.33$), which exhibits a ($\sqrt{3} \times \sqrt{3}$)R30° superstructure in low-energy electron diffraction (LEED) experiments. The Pt₃Sn/Pt(111) surface alloy ($\Theta_{\text{Sn}} = 0.25$), which requires the

diffusion of excess Sn into the platinum bulk, is formed around 1000 K and shows a $p(2 \times 2)$ LEED pattern.

Both surface alloys exhibit different electronic and geometric properties, which govern the improvement of the catalytic properties as compared to pure Pt(111). According to I/V-LEED studies of Atrei et al.,¹³ an outward relaxation of the Sn of 30 pm on Pt₃Sn/Pt(111) and of 23 pm on Pt₂Sn/Pt(111) is measured. Moreover the electronic structure is changed drastically by the alloying. In particular, STM experiments suggest a lowering of the local density of states (LDOS) at the Fermi level.¹⁴ According to density functional theory (DFT) calculations,²³ this is correlated with a downshift of the d-band center and a negative polarization of Pt due to the presence of Sn. Despite the fact that Sn is often considered a pure site blocker,²⁰ we were recently able to show that it is an important binding site for the α,β -unsaturated aldehydes, which, from the oxophilic character of Sn, generally require an O–Sn bond to form stable adsorption structures on Pt–Sn alloys.^{15,24}

The adsorption of crotonaldehyde on Pt(111) or Pt–Sn alloys was previously investigated experimentally^{2,8–12,16,24–28} and theoretically^{23,24,29–31} in several works.

Temperature-programmed desorption (TPD) and reflection–absorption infrared spectroscopy (RAIRS) measurements by de Jesús et al. indicate flat adsorption geometries for crotonaldehyde on Pt(111).²⁶ Although the measured shifts of the vibrational bands in their experiments suggest that crotonaldehyde exhibits a strong $\text{di}\sigma(\text{CC})$ interaction with the surface, no clear conclusion toward the adsorption geometries could be drawn. After providing thermal activation energy, these authors found a decarbonylation reaction forming propylene and CO, which desorb subsequently around 340 and 440 K. Moreover, H₂ desorption was measured in two steps at 280 and 440 K.

Other studies on crotonaldehyde reveal a complex adsorption behavior. Combined X-ray photoelectron spectroscopy (XPS) and DFT studies by Janin et al. point to an η^3 adsorption configuration of crotonaldehyde on Pt(111) with an interaction through the C=C bond and aldehydic oxygen.^{16,27} The alloying effect of Sn is observed in a strong decrease of calculated adsorption energies accompanied by a change of the preferred adsorption structure. On Pt₃Sn, these authors propose a mixed phase of an η^3 adsorption structure with an O–Sn interaction and a vertical form bonded only by the oxygen (η^1 -top-OSn), which becomes abundant on Pt₂Sn.

Recently Jerdev et al. probed the hydrogenation reaction of crotonaldehyde by employing XPS, LEED, and gas chromatographic analysis, finding that the selectivity on Pt(111), Pt₃Sn, and Pt₂Sn at the chosen reaction conditions is similar.² Therefore, these authors suggest that the selectivity of the hydrogenation is not solely due to the Sn–Pt alloy formation.

We present here the details of our studies on the crotonaldehyde adsorption on Pt(111) and on the Pt₃Sn/Pt(111) and Pt₂Sn/Pt(111) surface alloys. The previous investigations on crotonaldehyde and prenal^{15,24} showed that the multifunctional α,β -unsaturated aldehydes are able to adopt a variety of energetically competitive adsorption structures, which is enlarged when the alloying of Pt(111) with Sn is considered. Because of the small differences in relative stability, these configurations may coexist in disordered adsorbate phases on the surfaces, leading to a high complexity in the interpretation of the measured high-resolution electron energy loss spectroscopy (HREEL) spectra. Therefore, we have chosen to analyze the HREEL spectra by means of extensive DFT calculations of all conceivable adsorption structures of crotonaldehyde.

The identification of the actually present adsorption structures opens the way for a full characterization of the vibrational fingerprints, bonding mechanisms, and alloying effects and provides access to the reaction pathways leading to the desorption of the products or the deactivation of the catalysts. With the knowledge of the energetics of the elementary steps, it is possible to set up microkinetic models, which are useful tools for understanding the activities and selectivities of such complex catalytic processes such as the hydrogenation of α,β -unsaturated aldehydes.³²

2. Experimental Details

High purity crotonaldehyde (99.9+% purity, Aldrich Chemical Co.) was dosed onto the surfaces at 90–100 K. Prior to use it was purified by several freeze–pump–thaw cycles. All exposures are given in Langmuir units ($1 L = 1.33 \times 10^{-4}$ Pa s).

The disk-shaped Pt(111) crystal (MaTeck, Jülich) was cleaned with standard UHV ion bombardment (2.5 μA , 1 KeV, $T = 900$ K, 10 min) and annealing (1150 K for 5 min) cycles. The cleanliness and surface quality was controlled by Auger electron emission spectroscopy (AES), HREELS, and LEED. In case of larger carbon contamination, the crystal was annealed at 800 K at an oxygen pressure of 1×10^{-5} Pa before flashing to 1150 K.

The PtSn/Pt(111) surface alloys were prepared by Sn deposition at 300 K and subsequent annealing to ~ 650 –725 K or to 1025 K to form the Pt₂Sn(111)/Pt(111) and Pt₃Sn(111)/Pt(111) superstructures, respectively. The temperature ranges chosen depend on the amount of initially deposited Sn, which was determined by the Auger peak ratio of the Sn transition at 430 eV and the Pt signal at 237 eV.¹⁵ These surface alloys are characterized by $(\sqrt{3} \times \sqrt{3})R30^\circ$ and $p(2 \times 2)$ LEED patterns (Figure 1).

For the TPD experiments, a linear heating rate of 2 K/s was chosen. The crystal was placed in line of sight of the QMS ionizer with a distance of 1 mm to the front of the QMS aperture, which effectively attenuated background contributions.

With most of the possible adsorption structures being of C_1 symmetry (except the η^1 configurations) on the considered surfaces, the excitation of all vibrational normal modes becomes symmetry allowed in the dipolar regime. Thus, the HREELS spectra were recorded only in the specular reflection mode at an angle of 60° off the surface normal (primary electron energy of $E_0 = 4.7$ eV). Generally, an energy resolution (fwhm) between 25 and 35 cm^{-1} was obtained in the experiments, and all spectra were normalized to the elastic peak intensity.

Further details on the experimental setup and procedures are given in ref 15.

3. Computational Details

First, the four isomers of crotonaldehyde have been characterized in the gas phase using the resolution-of-the-identity³³ density functional theory (RI-DFT) of the Turbomole 5 program package.³⁴ The Becke–Perdew 86 functional^{35–37} and the Karlsruhe TZVP basis sets for C, O, and H have been employed for the vibrational calculations. The convergence of the relative stabilities has been confirmed by computations with the smaller SVP and the more flexible TZVPP basis sets. The vibrational spectra have been obtained by numerical computation of the second derivatives. Additional total energy calculations have been carried out with the coupled-cluster CCSD(T) approach implemented in the Molpro 2000³⁸ package employing correlation-consistent cc-pVDZ basis sets³⁹ (valence double- ζ basis sets augmented by polarization functions).

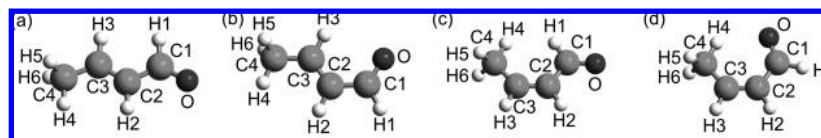


Figure 2. Schematic view of the gas phase isomers of crotonaldehyde (2-butenal): (a) *E*-(*s*)-*trans*, (b) *E*-(*s*)-*cis*, (c) *Z*-(*s*)-*trans*, and (d) *Z*-(*s*)-*cis*.

The DFT calculations on the model catalyst surfaces have been performed with the VASP code^{40,41} with the Perdew–Wang 91 functional⁴² (PW91, generalized gradient level) using the projected augmented wave (PAW) method.⁴³ A tight convergence of the plane wave expansion has been ensured with a cutoff of 400 eV.

All three-dimensional (3D) supercells were constructed from 4 layer thick metallic slabs (nearest neighbor distance of 2.82 Å, experimentally 2.77 Å) with a 5 layer vacuum above the surface and the adsorption of the molecule on one side. For Pt(111) and Pt₂Sn(111)/Pt(111), we have chosen a medium coverage situation modeled by 3 × 3 supercells (coverage 1/9 ML), for which the two-dimensional (2D) Brillouin zone integration is performed on a well-converged 3 × 3 × 1 *k*-point grids. The Pt₃Sn(111)/Pt(111) surface alloy has been modeled from a slightly larger (2√3 × 2√3)R30° cell (3 × 3 × 1 *k*-point grid, coverage 1/12 ML). In the latter cases, monolayers of the Pt–Sn alloys have been deposited above a 3 layer thick slab of Pt(111).²³ The corresponding relaxed clean PtSn surfaces show increased Pt–Sn distances of 2.86 Å, which originate from the larger covalent radius of Sn and lead to an outward relaxation of the Sn atoms [0.27 Å on Pt₂Sn(111)/Pt(111) and 0.31 Å on Pt₃Sn(111)/Pt(111)]. In order to compensate electrostatic interactions between the periodic slab images caused by the one-sided adsorption, a dipole correction has been applied to the potential and total electronic energies.

During the geometry optimizations, the two uppermost metal layers and the adsorbed molecule have been fully relaxed. For the vibrational analysis, the numerical computation of the second derivatives of the potential energy surface was used (indicating which atoms were included in the dynamic space). This does not include the negligible coupling between molecular high frequency modes and surface phonons. The HREELS loss intensities were derived from the dynamical dipole moments along the surface normal multiplied by an instrumental specific function and the inverse of the loss frequency.

For further details regarding our theoretical analysis, refer to ref 15.

4. Results and Discussion

4.1. Characterization of the Gas Phase Isomers of Crotonaldehyde. Crotonaldehyde exists in four rotational isomers in the gas phase: the *E*-(*s*)-*trans*, *E*-(*s*)-*cis*, *Z*-(*s*)-*trans*, and the *Z*-(*s*)-*cis* forms (Figure 2). These four rotational isomers differ in the relative position of the methyl group with respect to the aldehydic group at the C=C double bond (*E* or *Z*) and the orientation of the C=O moiety relative to the C=C double bond along the connecting single bond [(*s*)-*trans* or (*s*)-*cis*]. The isomerization of crotonaldehyde is also encountered on the surfaces, leading to huge sets of complex adsorption structures, which have to be considered on the three model catalyst surfaces.

Before switching to the DFT results related to the adsorption, theoretical investigations of crotonaldehyde in the gas phase have been performed using a periodic DFT approach (VASP^{40,41}) and a molecular code using localized basis functions (Turbo-

TABLE 1: Stabilities of the Four Rotational Isomers of Crotonaldehyde (Gas Phase) at Various Levels of Theory Relative to Its *E*-(*s*)-*trans* Form

relative energies	<i>E</i> -(<i>s</i>)- <i>trans</i> (kJ/mol)	<i>E</i> -(<i>s</i>)- <i>cis</i> (kJ/mol)	<i>Z</i> -(<i>s</i>)- <i>trans</i> (kJ/mol)	<i>Z</i> -(<i>s</i>)- <i>cis</i> (kJ/mol)
RI-BP86/SVP	0.0	4.5	10.1	9.0
RI-BP86/TZVP	0.0	7.8	11.4	14.5
RI-BP86/TZVPP	0.0	8.9	11.8	15.5
VASP	0.0	9.0	12.1	15.8
CCSD(T)/cc-pVDZ	0.0	8.9	11.8	15.5

mole³⁴). These results represent the references for the analysis of bond and frequency changes upon interaction with the substrates and for the interpretation of physisorbed multilayers. Because the differences in the relative stabilities obtained by DFT are rather small, extensive coupled cluster CCSD(T) computations have also been performed in order to evaluate the quality of the DFT results.

The *E*-(*s*)-*trans* rotational isomer is always the most stable form at all levels of theory (Table 1), followed by the slightly less stable *E*-(*s*)-*cis* crotonaldehyde. Depending on the size of the basis set, the *Z*-(*s*)-*trans* and *Z*-(*s*)-*cis* isomers follow in energy. As seen from Table 1, the step from a SVP basis to a TZVP basis affects primarily the relative stability of the *E*-(*s*)-*cis* and *Z*-(*s*)-*cis* rotational isomers. A more flexible basis set with an additional polarization function (the TZVPP basis) slightly enhances this effect. Because the relative stabilities converge to errors of about 1 kJ/mol with respect to the size of the basis set, the TZVP results represent a good compromise between accuracy and computational cost.

The results obtained with periodic plane wave DFT (VASP) in a large vacuum box of a 20 Å³ × 13 Å³ × 13 Å³ volume are of a similar quality as the RI-DFT/TZVPP calculations, giving the correct stability sequence. Again *E*-(*s*)-*trans* is the most stable rotational isomer, and the *E*-(*s*)-*cis* (9.0 kJ/mol), *Z*-(*s*)-*trans* (12.1 kJ/mol), and the *Z*-(*s*)-*cis* (15.8 kJ/mol) forms are calculated somewhat higher in relative energy. Our results compare well to previous calculations and experiments by other groups. MNDO/AM1 calculations performed by Thakur et al.⁴⁴ put the energy of *E*-(*s*)-*cis* crotonaldehyde 0.1 kJ/mol above the *E*-(*s*)-*trans* form, while experimental studies estimate the difference to be between 7.1 kJ/mol⁴⁵ and 8.1 kJ/mol.⁴⁶

The insertion of the relative stabilities from CCSD(T)/cc-pVDZ in a Boltzmann Ansatz provides an estimate of the composition of the crotonaldehyde gas phase at room temperature. At 300 K, about 98.4% of crotonaldehyde is in the *E*-(*s*)-*trans* form, while the rest is composed of 1% *E*-(*s*)-*cis*, 0.4% *Z*-(*s*)-*trans*, and 0.2% *Z*-(*s*)-*cis*. Using the results from the RI-DFT BP-86/TZVPP optimization, the value of *E*-(*s*)-*cis* crotonaldehyde increases to 2.7%, but the sum of the fractions of both *Z*-configured rotational isomers remains far below 1%. Therefore, it can be expected that *E*-(*s*)-*trans*- and *E*-(*s*)-*cis*-configured adsorption geometries will be most important on the various surfaces, which will be confirmed in the following sections.

Another important question involves the rotations around the C1–C2 and the C2=C3 bond axes, which transform the (*s*)-

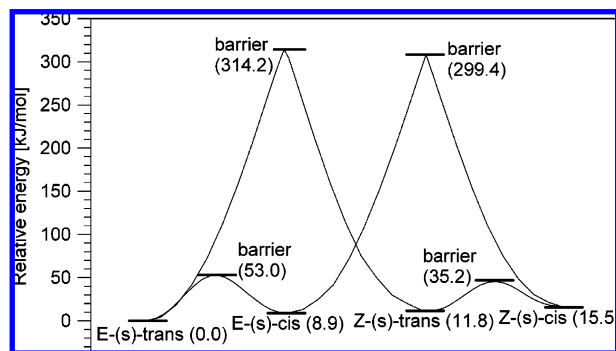


Figure 3. Computed potential energy curves (kJ/mol) for the conversion of the four rotational isomers (gas phase) by rotations around the C1–C2 [(s)-*trans* and (s)-*cis*] and the C2=C3 (*E* and *Z*) bonds.

trans into (s)-*cis* and the *E* into *Z* configurations, respectively. The complete potential curves of both rotations have been calculated at the RI-DFT BP-86/TZVP and TZVPP levels to determine the activation barriers. Additional single-point computations of the transition states at the geometries obtained by the RI-DFT BP-86/TZVPP calculations carried out at the CCSD(T)/cc-pVDZ level give more precise estimates of the activation barriers. The transition states are found at rotation angles of $\pm 90^\circ$ around the considered axis and are characterized by a single imaginary frequency corresponding to a rotation around this axis.

With a TZVP basis, the energy barrier of the rotation around the C1–C2 axis transforming *E*-(s)-*trans* crotonaldehyde into the *E*-(s)-*cis* form is computed at 44.8 kJ/mol (TZVPP 53.0, Figure 3) relative to the *E*-(s)-*trans* ground state. For the similar rotation of the *Z*-(s)-*trans* into the *Z*-(s)-*cis* rotational isomer, a somewhat lower activation barrier of 32.3 kJ/mol (TZVPP 35.2) relative to *Z*-(s)-*trans* has to be crossed. In agreement with the fact that the C1–C2 bond is a conjugating single bond, these activation barriers correspond to bond orders intermediate between a single and a double bond.

A comparison of the barrier heights at the HF, CCSD, and CCSD(T)/cc-pVDZ levels shows the importance of expanding the single reference configuration into the larger Hilbert space of singly and doubly excited configurations. While at the HF level, only 28.0 kJ/mol [*E*-(s)-*trans* to *E*-(s)-*cis*] and 9.8 kJ/mol [*Z*-(s)-*trans* to *Z*-(s)-*cis*] are computed for the activation energies, and these values increase substantially at the CCSD level to 37.1 and 22.6 kJ/mol (both 1.89×10^6 CSFs). Finally, with the perturbative triple excitations of CCSD(T), values of 41.0 and 27.6 kJ/mol are obtained for the two transition states. Thus, a consistent picture is found together with the RI-DFT results.

If the energies of both transition states are calculated relative to *E*-(s)-*trans* crotonaldehyde, the two structures appear very close in energy at 41.0 and 39.4 kJ/mol, respectively. This value of 40 kJ/mol can therefore be taken as a rough estimate of the contribution from the conjugation of the C1=O and C2=C3 double bond, which is broken in the transition state geometry.

The barriers of the rotations around the C2=C3 double bond are much higher. The barrier for transformation of the *E*-(s)-*trans* into the *Z*-(s)-*trans* rotational isomer at the TZVP level amounts to 328.0 kJ/mol (TZVPP 324.6 kJ/mol) relative to *E*-(s)-*trans*, and the one from *E*-(s)-*cis* into *Z*-(s)-*cis* is computed at 310.8 kJ/mol (TZVPP 309.2 kJ/mol). The activation barriers of the rotations around both bond axes are thus much larger, and no conversion between the four rotational isomers in the gas phase is expected in the electronic ground state at room

temperature. Nonetheless, these conversions may become possible upon adsorption onto a surface by transforming the C2=C3 double bond into an almost C2–C3 single bond.

For the activation energy of the rotation around the conjugating C1–C2 axis, Thakur et al. find a smaller rotational barrier of 8.9 kJ/mol (MNDO/AM1).⁴⁴ This finding does not match with the experimental results of 30.9 kJ/mol by De Groot et al.⁴⁶ and 68.6 kJ/mol by Durig et al.⁴⁵ The value of 42.4 kJ/mol computed at the CCSD(T) level for the transformation from *E*-(s)-*trans* crotonaldehyde to the *E*-(s)-*cis* isomer shows a better agreement with the experimental study by De Groot et al. It also appears that the rotational barrier obtained by Thakur et al. using a forcefield method results in a wrong barrier by 1 order of magnitude.

By adsorption of a large dose of crotonaldehyde onto Pt(111) or onto the two Pt–Sn surface alloys at 100 K, a multilayer phase can be formed. As we have shown recently,¹⁵ it can be well-approximated by a condensed phase. All rotational isomers of crotonaldehyde belong to the molecular point group C_s , and therefore, their 27 fundamental vibrations may be divided into 18 normal modes of A' symmetry and 9 modes of A'' symmetry. The specific assignments obtained from the vibrational analysis of the normal modes in the gas phase are presented in Tables 2 and 3.

In Figure 4 the comparison of a HREELS experiment of 4.5 L crotonaldehyde on Pt(111) with the calculated IR spectra of the four crotonaldehyde rotational isomers (RI-DFT BP86/TZVP level) is depicted. Most of the experimental peaks can be assigned to IR-active vibrational modes of *E*-(s)-*trans* crotonaldehyde in line with the larger abundance of this species in the gas phase (Table 2). However, one has to keep in mind that unless the multilayers of crotonaldehyde are disordered and, therefore, the molecular orientations are isotropic, IR intensities cannot be compared directly to the HREELS intensities. Furthermore, the IR intensities are decreased by a frequency-dependent damping factor that is proportional to ω^{-1} .⁴⁷ The vibrational spectra can be divided into six frequency regions with distinct types of normal modes. Between 3100 cm^{-1} and 2700 cm^{-1} , the $\nu(\text{C–H})$ stretching region is located, followed between 1800 cm^{-1} and 1500 cm^{-1} by the $\nu(\text{C=O})$ and $\nu(\text{C=C})$ double-bond stretching modes. From 1460 cm^{-1} to about 1250 cm^{-1} , the region of the in-plane (A') and out-of-plane (A'') $\delta'(\text{CH})$ and $\delta''(\text{CH})$ deformation vibrations and the umbrella mode $\nu(\text{CH}_3)$ extends. The characteristic stretching vibrations $\nu(\text{C–C})$ of the carbon skeleton or chain are typically found around 1100 cm^{-1} , whereas the other typical normal modes of the molecular backbone, namely, the $\delta(\text{OCC})$, $\delta(\text{CCC})$ and the various torsion modes $\tau(\text{C–C, CH}_3)$, lie below 650 cm^{-1} . Mainly, the out-of-plane A'' symmetric deformation modes of the $\gamma(\text{CH})$ type range from about 1050 cm^{-1} to 700 cm^{-1} .

The numerical frequencies from the vibrational analysis with VASP and the molecular RI-DFT computations match very well. The differences in the frequencies for a given structure vary by less than 10 cm^{-1} ($<1.5\%$), although a few unsystematic exceptions are noticed (for example, the aldehydic $\nu(\text{C1–H1})$ stretching frequencies, Table 2).

Concerning experimental references of previous IR and Raman studies, the agreement of our computed frequencies is best with the data measured by Durig et al.⁴⁵ in liquid phase (Table 2), but the gas phase frequencies of Oelichmann et al.⁴⁸ are also very close. Typically, at the harmonic approximation, the frequencies of the $\nu(\text{C–H})$ stretching modes are overestimated by about 15 to 70 cm^{-1} (i.e., 1–2%) in the numerical

TABLE 2: Computed Gas Phase Frequencies (VASP and Turbomole), IR Oscillator Strengths (Turbomole, atomic units), and Assignment of the Normal Modes of *E*-(*s*)-*trans* and *E*-(*s*)-*cis* Crotonaldehyde Compared to a Measured HREELS Multilayer Spectrum^a

<i>E</i> -(<i>s</i>)- <i>trans</i>					<i>E</i> -(<i>s</i>)- <i>cis</i>					experimental data				
VASP	RI-DFT/BP86/TZVP				VASP	RI-DFT/BP86/TZVP				liquid ⁴⁸	MNDO ⁴⁴	MNDO ⁴⁴	gas phase ⁴⁵	HREELS multilayer, this work
ω (cm ⁻¹)	ω (cm ⁻¹)	int	sym	assignment	ω (cm ⁻¹)	ω (cm ⁻¹)	int	sym	assignment	ω (exp) (cm ⁻¹)	ω (calc) (cm ⁻¹)	assignment	ω (exp) (cm ⁻¹)	ω (exp) (cm ⁻¹)
3097	3088	8.4	A'	ν (C2-H2)	3082	3077	23.4	A'	ν (C2-H2)	3058	3049	$\nu_{as}(\text{CH})$	3058	3042
3067	3064	23.8	A'	ν (C4-H4)	3075	3068	2.2	A'	ν (C3-H3)	2995	3005	$\nu_s(\text{CH})$	2995	3002
3042	3044	1.8	A'	ν (C3-H3)	3053	3043	11.1	A'	ν (C4-H4)	2980	2967	$\nu_{as}(\text{CH}_3)$	2980	2982
3007	3016	8.6	A''	$\nu_{as}(\text{C4-H5,6})$	3004	2994	8.7	A''	$\nu_{as}(\text{C4-H5,6})$	2963	2967	$\nu_{as}(\text{CH}_3)$	2963	2944
2965	2966	10	A'	$\nu_s(\text{CH}_3)$	2965	2951	9.9	A'	$\nu_s(\text{CH}_3)$	2938	2940	$\nu_s(\text{CH}_3)$	2938	2916
2789	2766	121.9	A'	ν (C1-H1)	2817	2800	177.6	A'	ν (C1-H1)	2805 (2728)	2789	ν (CH-Ald.)	2725	2727
1706	1698	283.9	A'	ν (C=O)	1713	1710	83.7	A'	ν (C=O)	1720	1732	ν (C=O)	1720	1693
1642	1640	61.6	A'	ν (C=C)	1621	1620	240.8	A'	ν (C=C)	1649	1665	ν (C=C)	1649	1641
1433	1435	23.6	A'	$\delta'(\text{CH}_3)$	1433	1439	37.8	A'	$\delta'(\text{CH}_3)$	1455	1441	$\delta_{as}(\text{CH}_3)$	1455	1444
1426	1433	11.1	A''	$\delta''(\text{CH}_3)$	1427	1431	10.5	A''	$\delta''(\text{CH}_3)$	1455	1439	$\delta_{as}(\text{CH}_3)$	1455	1444
1369	1373	2.7	A'	δ (C1H1)	1382	1390	3.2	A'	δ (C1H1)	1391	1406	$\delta_{as}(\text{CH}_3)$	1391	1389
1357	1359	7.8	A'	ν (CH ₃)	1355	1365	4.6	A'	ν (CH ₃)	1375	1382	ρ (CH-Ald.), ρ (CH-Ald.), $\delta_{as}(\text{CH}_3)$	—	1375
1287	1289	3.9	A'	δ (C3H3)	1284	1286	8.1	A'	$\delta_s(\text{C2H2-C3H3})$	1304	1291	δ (CH)	1304	1305
1238	1236	0.3	A'	δ (C2H2)	1274	1277	18.7	A'	$\delta_{as}(\text{C2H2-C3H3})$	1253	1233	δ (CH)	1252	1253
1143	1132	66.2	A'	ν (C1-C2)	1119	1113	3.4	A'	ν (C3-C4)	1147	1127	ν (C-C)	1147	1147
1078	1058	10.8	A'	ν (C3-C4)	1038	1038	2.5	A''	$\gamma'(\text{CH}_3)$	1074	1056	ν (C-CH ₃)	1074	1075
1029	1028	1.6	A''	$\gamma''(\text{CH}_3)$	1008	1003	10.7	A'	ν (C1-C2)	1042	1062	ρ (CH ₃)	1030	1042
987	991	10.1	A''	γ (C1H1)	989	995	0.9	A''	γ (C1H1)	973	986	ρ (C-CH ₃)	973	966
965	967	31.1	A''	$\gamma_s(\text{C2H2-C3H3})$	970	975	33.8	A''	$\gamma_s(\text{C2H2-C3H3})$	973	983	τ (CCH), ρ (CH)	928	931
915	906	30.2	A'	$\gamma'(\text{CH}_3)$	871	868	39.6	A'	$\gamma'(\text{CH}_3)$	928	926	ρ (CH-Ald.)	780	780
769	769	0.02	A''	$\gamma_{as}(\text{C2H2-C3H3})$	747	750	0.1	A''	$\gamma_{as}(\text{C2H2-C3H3})$	780	762	ω (CCH)	730	727
526	531	7.4	A''	δ (O-C1C2)	725	726	37.9	A'	δ (O-C1C2)	539	535	δ (CCO)	554	542
452	448	2.6	A'	δ (C2=C3-C4)	386	385	2.5	A'	δ (C2=C3-C4)	464	484	δ (CCC), ρ (CCCH ₃)	454	459
292	295	7.6	A''	τ (C2=C3)	225	238	3.3	A''	τ (C2=C3)	295	289	τ (CCH), ω (CCH)	295	297
198	203	6.1	A'	δ (C1-C2=C3)	206	199	1.4	A''	τ (CH ₃)	230	231	δ (CCCH ₃), δ (CCC)	211	216
176	170	1	A''	τ (CH ₃)	197	197	5.1	A'	δ (C1-C2=C3)	173	187	τ (C-CH ₃)	139	145
137	110	0.6	A''	τ (C1-C2)	134	146	6	A''	τ (C1-C2)	122	114	τ (CHO)	122	—

^a The assignments obtained from both computational methods are identical.

calculations. In the region below 2000 cm⁻¹, a much better accuracy is achieved.

However, slight discrepancies in the assignments and normal coordinate analysis given by both groups are found such that the measured signals at 2805 and 2728 cm⁻¹⁴⁸ as well as 2808 and 2725 cm⁻¹⁴⁵ were assigned in different manners to vibrations of the *E*-(*s*)-*trans* isomer by Durig et al. and Oelichmann et al. While the latter authors considered that the band at 2805 cm⁻¹ arises from the stretching mode ν (C1-H1) of the aldehydic hydrogen,⁴⁸ Durig et al. had previously assigned the signal at a lower frequency 2725 cm⁻¹ to this normal mode; the other signals, respectively, were concluded to arise from combination tones. In a more recent combined experimental and theoretical study carried out by IR and Raman spectroscopy and a normal coordinate analysis in the valence force field approximation, Thakur et al.⁴⁴ supported the assignments of Oelichmann et al.⁴⁸ The values of 2789 and 2766 cm⁻¹ obtained here using VASP and RI-DFT, respectively, are in better agreement with the experimental bands around 2805 cm⁻¹; hence, we attribute this band to the ν (C1-H1) stretching mode.

Another discrepancy is disclosed in the low frequency region. At 730 cm⁻¹ (gas phase) and 727 cm⁻¹ (liquid), a band was assigned by Durig et al. to the γ (C1-H1) wagging mode, but our present results put this normal mode at 987 cm⁻¹.

The identification of the four crotonaldehyde rotational isomers in the gas phase is possible by certain combinations of

vibrational normal modes, which are influenced characteristically by the configuration along the C2=C3 double bond or along the conjugating C1-C2 single bond. Thus, for instance, the moderately intense $\gamma_s(\text{C2H2-C3H3})$ vibrations at 967 cm⁻¹ [*E*-(*s*)-*trans*] and 975 cm⁻¹ [*E*-(*s*)-*cis*] are characteristic for the *E* configuration, while the somewhat weaker bands 1230 cm⁻¹ [*Z*-(*s*)-*trans*] and 1246 cm⁻¹ [*Z*-(*s*)-*cis*] assigned to $\delta_s(\text{C2H2-C3H3})$ might identify the *Z* configuration. The differentiation between the (*s*)-*trans* and the (*s*)-*cis* forms is possible by several bands. Namely, the set of bands at 1132 cm⁻¹ [ν (C1-C2)], 1640 cm⁻¹ [ν (C2=C3)], and 1698 cm⁻¹ [ν (C1=O)] *E*-(*s*)-*trans* and 1131 cm⁻¹, 1634 cm⁻¹, and 1685 cm⁻¹ (*Z*-(*s*)-*trans*) is specific for the (*s*)-*trans* configuration. In contrast, the bands at 868 cm⁻¹ [$\gamma'(\text{CH}_3)$], 1620 cm⁻¹ [ν (C2=C3)], and 1710 cm⁻¹ [ν (C1=O)] *E*-(*s*)-*cis* as well as the corresponding bands at 851 cm⁻¹, 1609 cm⁻¹, and 1702 cm⁻¹ (*Z*-(*s*)-*cis*) allow an identification of the (*s*)-*cis* forms. The weakly separated bands at 726 and 721 cm⁻¹ (or also 2800 and 2812 cm⁻¹) can be adducted additionally for the differentiation. The first low-lying signals indicate one of either the *E*-(*s*)-*cis* or the *Z*-(*s*)-*trans* forms, while signals around 2766 and 2789 cm⁻¹ point toward the *E*-(*s*)-*trans* or *Z*-(*s*)-*cis* rotational isomers.

4.2. Crotonaldehyde on Pt(111). 4.2.1. TPD: Chemisorbed States and Evolution with Temperature. Crotonaldehyde shows a complex fragmentation pattern after electron impact ionization, which results in particular in intense signals at $m/z = 70, 69,$

TABLE 3: Computed Gas Phase Frequencies (VASP and Turbomole), IR Oscillator Strengths (Turbomole, atomic units), and Assignment of the Normal Modes of Z-(s)-trans and Z-(s)-cis Crotonaldehyde Compared to a Measured HREELS Multilayer Spectrum^a

Z-(s)-trans					Z-(s)-cis				
VASP	RI-DFT/BP86/TZVP				VASP	RI-DFT/BP86/TZVP			
ω (cm ⁻¹)	ω (cm ⁻¹)	int	sym	assignment	ω (cm ⁻¹)	ω (cm ⁻¹)	int	sym	assignment
3101	3097	10.0	A'	ν (C2-H2)	3106	3098	5.7	A'	ν (C4-H4)
3082	3075	17.9	A'	ν (C4-H4)	3091	3081	18.1	A'	ν (C2-H2)
3057	3050	2.6	A'	ν (C3-H3)	3054	3044	11.2	A'	ν (C3-H3)
3013	3003	8.4	A''	ν_{as} (C4-H5,6)	3000	2992	9.4	A''	ν_{as} (C4-H5,6)
2976	2960	10.2	A'	ν_s (CH ₃)	2966	2951	9.5	A'	ν_s (CH ₃)
2825	2812	100.5	A'	ν (C1-H1)	2804	2789	184.8	A'	ν (C1-H1)
1687	1685	255.4	A'	ν (C=O)	1706	1702	104.0	A'	ν (C=O)
1634	1634	29.8	A'	ν (C=C)	1610	1609	150.8	A'	ν (C=C)
1435	1435	26.9	A'	δ' (CH ₃)	1438	1447	11.8	A''	δ'' (CH ₃)
1428	1434	10.1	A''	δ'' (CH ₃)	1418	1423	65.0	A'	δ' (CH ₃)
1406	1409	7.1	A'	δ (C1H1)	1404	1408	0.4	A'	δ (C1H1)
1364	1370	7.2	A'	ν (CH ₃)	1379	1385	11.3	A'	δ_{as} (C2H2-C3H3)
1333	1338	6.9	A'	δ_{as} (C2H2-C3H3)	1343	1348	14.7	A'	ν (CH ₃)
1228	1230	12.1	A'	δ_s (C2H2-C3H3)	1244	1246	5.2	A'	δ_s (C2H2-C3H3)
1136	1131	42.3	A'	ν (C1-C2)	1087	1090	1.1	A'	ν (C3-C4)
1033	1032	0.6	A''	γ'' (CH ₃)	1036	1036	0.6	A''	γ'' (CH ₃)
994	995	0.1	A''	γ (C1H1)	991	996	3.1	A''	γ (C1H1)
990	992	11.2	A'	γ' (CH ₃)	981	975	1.6	A''	γ_{as} (C2H2-C3H3)
971	973	4.0	A''	γ_{as} (C2H2-C3H3)	974	971	11.4	A'	ν (C1-C2)
911	906	20.2	A'	ν (C3-C4)	859	851	36.1	A'	γ' (CH ₃)
717	721	37.6	A''	γ_s (C2H2-C3H3)	781	785	43.3	A'	δ (O-C1C2)
599	600	1.5	A'	δ (O-C1C2)	678	683	28.1	A''	γ_s (C2H2-C3H3)
426	432	14.8	A'	δ (C2=C3-C4)	399	404	1.6	A'	δ (C2=C3-C4)
324	330	0.0	A''	τ (C2=C3)	340	348	0.6	A''	τ (C2=C3)
210	222	3.2	A'	δ (C1-C2=C3)	227	224	7.0	A'	δ (C1-C2=C3)
166	168	4.7	A''	τ (C1-C2)	147	148	6.9	A''	τ (CH ₃)
121	123	1.3	A''	τ (CH ₃)	78	84	1.7	A''	τ (C1-C2)

^a The assignments obtained from both computational methods are identical.

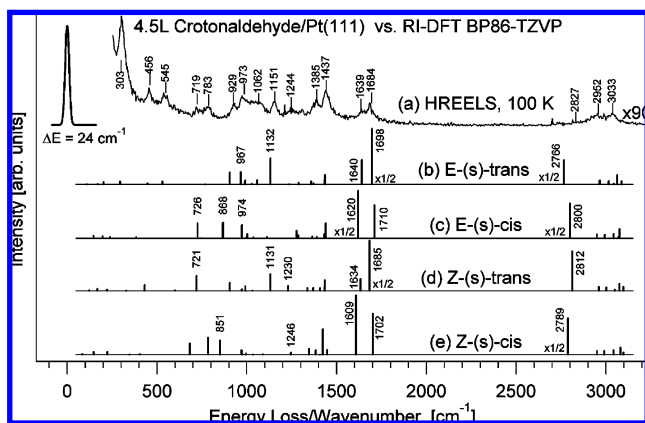


Figure 4. Comparison of the experimental HREELS spectrum of a multilayer composed on Pt(111) [(a) 4.5 L crotonaldehyde adsorbed at 100 K; specular mode, 60° angle to surface normal] and the computed IR spectra of (b) *E*-(s)-trans, (c) *E*-(s)-cis, (d) *Z*-(s)-trans, and (e) *Z*-(s)-cis gas phase crotonaldehyde (RI-BP86/TZVP).

41, 39, 28, and 2.⁴⁹ In order to identify any other potential product that may desorb after formation on the surface, full TPD spectra in the mass range 2–100 amu have been recorded between 100 and 800 K. Besides the parent ion ($m/z = 70$), which is always accompanied by the mentioned fragments, only the signals $m/z = 2$ and 28 appear independently and are, hence, the only decomposition products desorbing.

The evolution of the crotonaldehyde desorption states in TPD experiments recorded between 100 and 800 K with increasing exposures allows several conclusions on the adsorbed species that will be important later for interpretation of the HREELS data. At initial exposures below 1.5 L (Figure 5), no desorption

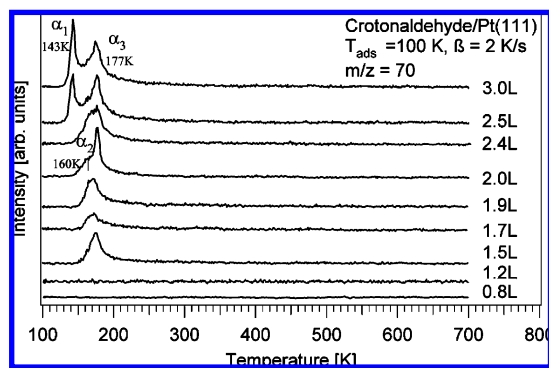


Figure 5. Crotonaldehyde TPD spectra ($m/z = 70$) after adsorption of different exposures on Pt(111) at 100 K. Three desorption peaks at 143, 160, and 177 K are distinguished.

signals of intact crotonaldehyde are observed, and an irreversibly adsorbed monolayer is formed. Increasing the exposure to about 1.9 L, the TPD series first shows a first-order desorption signal at 177 K (α_3) that may be interpreted as the desorption of a reversibly adsorbed species or a partial desorption process. Assuming a coverage independent pre-exponential factor of $\nu = 10^{13} \text{ s}^{-1}$, an activation barrier for the desorption process of $45.3 \pm 1.5 \text{ kJ/mol}$ is calculated by Redhead analysis⁵⁰ for this state (estimated errors of the size of $\Delta T \leq 4 \text{ K}$, $\Delta \beta \leq 0.1 \text{ K/s}$). At exposures between 2.0 L and about 2.4 L, a low-temperature shoulder of this desorption state is recognized at 160 K (α_2). Using the same assumptions, we estimated the activation barrier to be $41.9 \pm 1.5 \text{ kJ/mol}$. Starting at about 2.5 L, the growth of a desorption signal from a physisorbed multilayer is observed at 143 K. If again a zero-order kinetics is assumed, a desorption

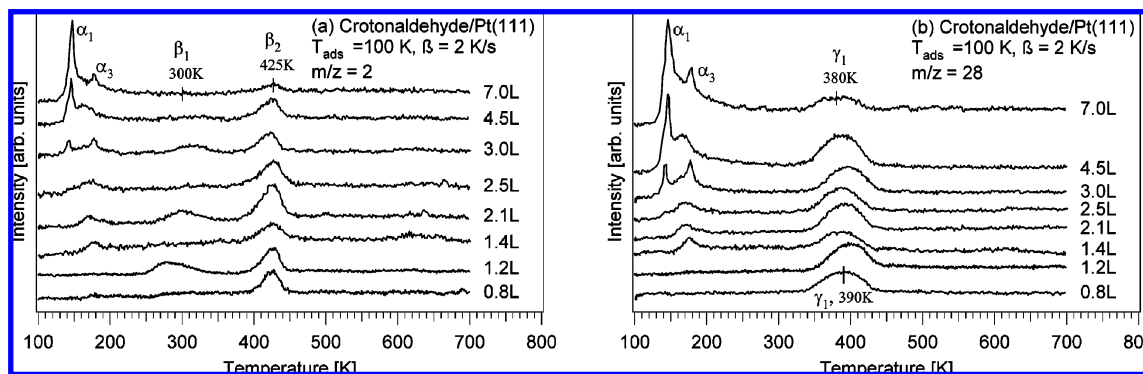


Figure 6. Evolution of desorbing H₂ originating from the decomposition of the strongly chemisorbed crotonaldehyde on Pt(111): (a) $m/z = 2$ and (b) CO $m/z = 28$.

activation energy of 34.9 ± 1.5 kJ/mol is found using the onset at ~ 140 K. This value is comparable to the standard vaporization enthalpy of $\Delta H_m(298.15 \text{ K}) = 37.70 \pm 0.12$ kJ/mol measured by Steele et al.⁵¹

The decomposition of the irreversibly adsorbed crotonaldehyde species above 300 K leads to desorption of H₂ ($m/z = 2$) and CO ($m/z = 28$) (Figure 6). In the TPD spectra for $m/z = 2$ (Figure 6a), two signals are noticed at ~ 300 and 425 K. The desorption-limited state β_1 around 300–315 K is rather weak and shifts sizably with crotonaldehyde coverage. We attribute this signal to the dissociation of the aldehydic hydrogen for strongly adsorbed crotonaldehyde structures, which must occur at temperatures below the onset of this desorption process. This conclusion is supported by the results from the CO TPD and our HREELS measurements, which is discussed below.

The desorption state β_2 around 425 K is always clearly identified, and its position is independent of the coverage. This state has been assigned to a reaction limited desorption process arising from the dehydrogenation of the surface species. Despite slight variations of this signal, the peak area also reaches saturation at exposures of about 1.4 L, in agreement with the dose determined for the irreversibly adsorbed monolayer.

Further support is gained from an exposure series and TPD spectra for $m/z = 28$ (Figure 6b). Apart from the CO signals originating from the fragmentation reaction of the crotonaldehyde parental ion in the mass spectrometer (α_1 and α_3), only a single desorption-limited state is measured that is even seen for very small crotonaldehyde exposures. The desorption rate maximum shifts slightly from about 390 K at low coverages to 380 K for exposures higher than ~ 1.4 L, when it also saturates. It is linked to the decomposition of the aldehydic function and thus supports our previous conclusion. An analysis of the activation energy for the desorption process of CO gives an estimate of 102.4 ± 1.5 kJ/mol at 0.8 L and 99.7 ± 1.5 kJ/mol at 2.1 L, which is in good agreement with TPD experiments of CO on Pt(111) performed by Paffet et al.,¹⁹ who measured CO desorption between 450 K (125 kJ/mol) and 375 K (108 kJ/mol) for increasing coverages.

Generally, our findings agree well with TPD studies reported by de Jesús et al. for an initial multilayer adsorption.²⁶ Besides multilayer desorption at 140 K, these authors measured the “monolayer” desorption state of intact crotonaldehyde as a wide signal with a maximum at 175 K and a high-temperature tail extending to 220 K. Also, the decarbonylation process on the Pt surface was observed, with desorption states of CO at 420 K and H₂ at 280 and 440 K, and very weak signals of 39 and 41 amu corresponding to a propylene desorption around 340 K have been reported by these authors. Some very weak traces of

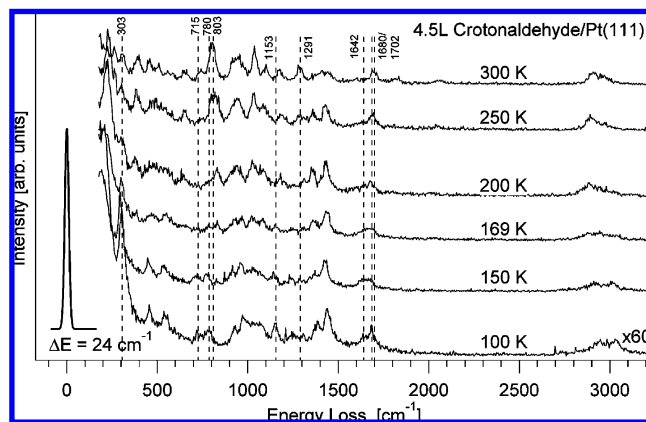


Figure 7. HREELS spectra of 4.5 L crotonaldehyde adsorbed onto Pt(111) at 100 K and after annealing to different temperatures ranging from 150 to 300 K (specular geometry, $E_0 = 4.7$ eV, $\Delta E = 24$ cm⁻¹).

these masses were also visible, evolving around ~ 330 K in our experiments.

Therefore, quite similar to our results on prenal/Pt(111),¹⁵ crotonaldehyde forms an irreversible monolayer at low temperatures, which decomposes in several sequential steps beginning around 275 K. For the initial dissociation of the aldehydic hydrogen, the activation energy must be slightly lower than the activation energy of the subsequent desorption processes starting at ~ 300 K and even much lower than the desorption energy of the irreversibly bonded crotonaldehyde species, which decompose here. Only small temperature shifts are observed for intact crotonaldehyde desorbing from several weakly bound states below 200 K, which implies only a weak coverage dependence of the adsorption energies (desorption activation energies).

4.2.2. Low-Temperature HREELS. As deduced from the TPD experiments, only intact crotonaldehyde species are expected to be present on Pt(111) from the adsorption in the temperature range of 100–250 K. If the initial exposure is chosen small enough, coverages can be formed which show only the low-temperature desorption states α_2 and α_3 in TPD (Figure 5). At very small coverages below ~ 1.2 L, the spectra are expected to arise from a phase of irreversibly bonded crotonaldehyde. After annealing, the desorption states are subsequently removed, so that the HREEL spectrum of 4.5 L crotonaldehyde shown in Figure 7 recorded after annealing to 200 K corresponds also to the irreversibly bonded forms.

The removal of the low-temperature desorption states $\alpha_1 - \alpha_3$ in the experiments leads mainly to an improvement of the overall shape of the HREEL spectra, slight changes in the relative loss intensities, and small shifts, but otherwise the

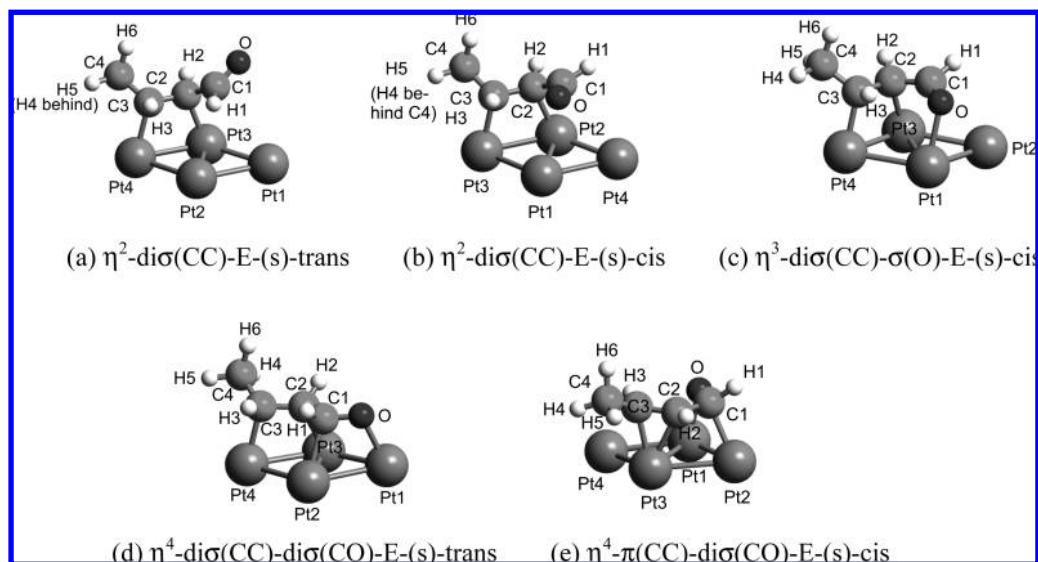


Figure 8. Optimized geometries of the five identified crotonaldehyde adsorption structures on Pt(111) (all structures have been obtained from DFT optimization at a theoretical coverage of 1/9 ML).

differences between the spectrum of the multilayer at 100 K and the spectra to 200 K are very small. Some small changes have been marked by dashed lines in Figure 7. Obviously, from the small differences found between 150, 169, and 200 K, the irreversibly adsorbed crotonaldehyde layer dominates the HREEL spectra in the low-temperature region.

Among the minor changes that can be noticed is the disappearance of a weak loss peak at 715 cm^{-1} (multilayer), whereas an additional signal at 831 cm^{-1} starts to develop. It can be recognized best at 200 K. Following the desorption of the reversible adlayer (α_3) at ~ 177 K, the HREEL spectrum also shows some differences in the frequency range between 500 and 1300 cm^{-1} , where at least six vibrational bands are found. At 200 K, the loss signals at 780 cm^{-1} and 1153 cm^{-1} , which seem to characterize the low-temperature adsorption states, are also no longer observed. Our extensive DFT calculations do not reflect these changes, suggesting that processes such as a partial desorption and a concomitant reordering of the adsorbates or phase changes may play a role here.

While the HREEL spectra recorded after annealing to 200 and 250 K are very similar, the data obtained at 300 K exhibits again important changes that are attributed to the start of the decomposition of the molecules. For instance, a $\nu(\text{C}=\text{O})$ stretching mode seen at 1680 cm^{-1} around 200 K shifts to ~ 1702 cm^{-1} , indicating the formation of new intermediates. The appearance of two peaks at 1823 and 2057 cm^{-1} can easily be assigned to bridge- and top-bonded CO,¹⁹ which arises from the decomposition of the aldehydes.

The DFT structure optimizations gave two sets of either strongly ($-55.3 \geq E_{\text{ads}} \geq -80.2$ kJ/mol, $\Theta = 1/9$ ML) or weakly bonded structures ($E_{\text{ads}} > -25$ kJ/mol), while a number of configurations were found to be unstable. Like in the case of prenal,¹⁵ the η^1 -top, η^2 -di σ (CO), and η^2 - π (CC) types are among the group of weakly bonded forms. Aside from their low adsorption energies, their computed HREELS fingerprints are incompatible with the experimental vibrational spectra between 150 and 300 K, which allows us to exclude them unambiguously. A further reduction of the possible candidates is achieved by excluding the rotational isomers that show high barriers for conversion from the most stable and abundant E-(s)-trans form (see discussion of gas phase properties), namely, all structures derived from the Z-(s)-trans and Z-(s)-cis isomers.

This is also supported by the experiments because their theoretical vibrational fingerprints do not match the experimental data satisfactorily.

As reported previously, we have identified the remaining five configurations of strongly bonded crotonaldehyde in the experimental HREELS data, i.e., two flat η^2 -di σ (CC), one η^3 , and two η^4 forms (Figure 8). These structures correspond directly to those found in the mixed phase of prenal/Pt(111). However, their chemisorption energy is 25% stronger. Table 4 gives an overview on the adsorption energies and the most important bond distances of these configurations.

Compared to the much smaller number of considered structures treated in a previous DFT study,²⁹ we considered the nearly full configuration space of initial coordination types in our present study. For the common structures of both studies, we find only slight deviations, despite the use of different pseudopotentials (US-PP versus PAW here) and the inclusion of the important corrections of the spurious dipole interactions between the periodical slabs during the geometry optimizations in this case.

Extending the assignments we have given in ref 24, Figure 9 presents a comparison of the experimental HREELS spectrum of strongly adsorbed crotonaldehyde with the computed fingerprints of the five retained structures. Although all experimental peaks have been essentially explained in our recent investigation using only the η^2 -di σ (CC)-E-(s)-trans, η^3 -di σ (CC)- σ (O)-E-(s)-cis, and η^4 -di σ (CC)-di σ (CO)-E-(s)-trans structures, the two additional η^2 -di σ (CC)-E-(s)-cis and η^4 - π (CC)-di σ (CO)-E-(s)-cis geometries exhibit related vibrational properties and similarly strong adsorption energies and, hence, must be taken into account. Their inclusion even improves the overall fit between the experimental and theoretical results. The width of the experimental peak at 1686 cm^{-1} is somewhat better reproduced when adding the $\nu(\text{C}1=\text{O})$ stretching modes of the η^2 -di σ (CC)-E-(s)-trans (1686 cm^{-1}) and η^2 -di σ (CC)-E-(s)-cis forms (1609 cm^{-1}).

Most of the experimental loss peaks measured below 1500 cm^{-1} can be assigned on the basis of the other structures. Thus, their interpretation remains consistent with the ones that we have identified previously. At large, in the interval between ~ 1430 and ~ 1200 cm^{-1} , all of $\delta(\text{CH})$ deformation modes are found, while in the range from ~ 1000 to ~ 740 cm^{-1} , the corresponding

TABLE 4: Adsorption Energies and Main Bond Distances for the Five Identified Adsorption Structures of Crotonaldehyde on Pt(111) Compared to the Bond Distances of the Two Corresponding Gas Phase Isomers

geometry	gas phase					Pt(111)				
	$E-(s)-trans$	$E-(s)-cis$	$\eta^2-di\sigma(CC)-E-(s)-trans$	$\eta^2-di\sigma(CC)-E-(s)-cis$	$\eta^3-di\sigma(CC)-\sigma(O)-E-(s)-cis$	$\eta^4-di\sigma(CC)-di\sigma(CO)-E-(s)-trans$	$\eta^4-\pi(CC)-di\sigma(CO)-E-(s)-cis$	$\eta^4-\pi(CC)-di\sigma(CO)-E-(s)-trans$	$\eta^4-\pi(CC)-di\sigma(CO)-E-(s)-cis$	$\eta^4-\pi(CC)-di\sigma(CO)-E-(s)-trans$
supercell			3×3	3×3	3×3	3×3	3×3	3×3	3×3	3×3
E_{ads} (kJ/mol)			-76.0	-73.6	76.9	-80.2	-68.7			
$r(O-C1)$ (Å)	1.23	1.23	1.22	1.24	1.27	1.33	1.34			
$r(C1-C2)$ (Å)	1.46	1.47	1.50	1.48	1.45	1.49	1.48			
$r(C2-C3)$ (Å)	1.35	1.35	1.50	1.49	1.49	1.49	1.42			
$r(C3-C4)$ (Å)	1.49	1.49	1.51	1.52	1.52	1.51	1.50			
$r(O-M)$ (Å)			—	—	2.26	2.12	2.12			
$r(C1-M)$ (Å)			—	—	—	2.22	2.19			
$r(C2-M)$ (Å)			2.14	2.13	2.19	2.16	2.28			
$r(C3-M)$ (Å)			2.14	2.15	2.12	2.14	2.21			

TABLE 5: Computed Frequencies of Important Vibrational Normal Modes of Crotonaldehyde Structures on Pt(111), $\Theta = 1/9$ ML

	Pt(111)						Pt(111)					
	$\eta^2-di\sigma(CC)-E-(s)-trans$	$\eta^2-di\sigma(CC)-E-(s)-cis$	$\eta^3-di\sigma(CC)-\sigma(O)-E-(s)-cis$	$\eta^4-di\sigma(CC)-di\sigma(CO)-E-(s)-trans$	$\eta^4-\pi(CC)-di\sigma(CO)-E-(s)-cis$	$\eta^4-top-E-(s)-trans$	$\eta^2-di\sigma(CC)-E-(s)-trans$	$\eta^2-di\sigma(CC)-E-(s)-cis$	$\eta^3-di\sigma(CC)-\sigma(O)-E-(s)-cis$	$\eta^4-di\sigma(CC)-di\sigma(CO)-E-(s)-trans$	$\eta^4-\pi(CC)-di\sigma(CO)-E-(s)-cis$	$\eta^4-top-E-(s)-trans$
supercell	3×3	3×3	3×3	3×3	3×3	3×3	3×3	3×3	3×3	3×3	3×3	3×3
$\nu(C-H)$ range	3046-2720	3042-2851	3042-2918	3047-2894	3047-2894	3088-2882						
$\nu(C1=O)$	1686	1610	1443	1172	1172	1562						
$\nu(C1-C2)$	1024	993	1025	988	988	1154						
$\nu(C2=C3)$	1115	1109	1111	1100	1100	1633						
$\nu(C3-C4)$	1069	1073	1074	1066	1066	1095						
$\nu_{as}(PtC2-PtC3)$	519	554	539	542	542	—						
$\nu_s(PtC2-PtC3)$	348	441	351	369	369	—						
$\nu(M-O)^b$	—	—	302	—	—	107						
$\nu_{as}(MO-PtCl)^c$	—	—	—	452	452	—						
$\nu_s(MO-PtCl)^c$	—	—	—	289	289	—						

^a Complex couplings to other vibrations are omitted for a sake of clarity. ^b This normal mode appears only for η^1 and η^3 configurations. ^c The η^4 configurations show four molecule-surface stretching modes, which are usually the coupled asymmetric and symmetric combinations of the Pt-C=C and Pt-C=O vibrations. Both coupled normal modes may be coupled, giving rise to four linear combinations, for example, in the case of the $\eta^4-\pi(CC)-di\sigma(CO)-(s)-cis$ form.

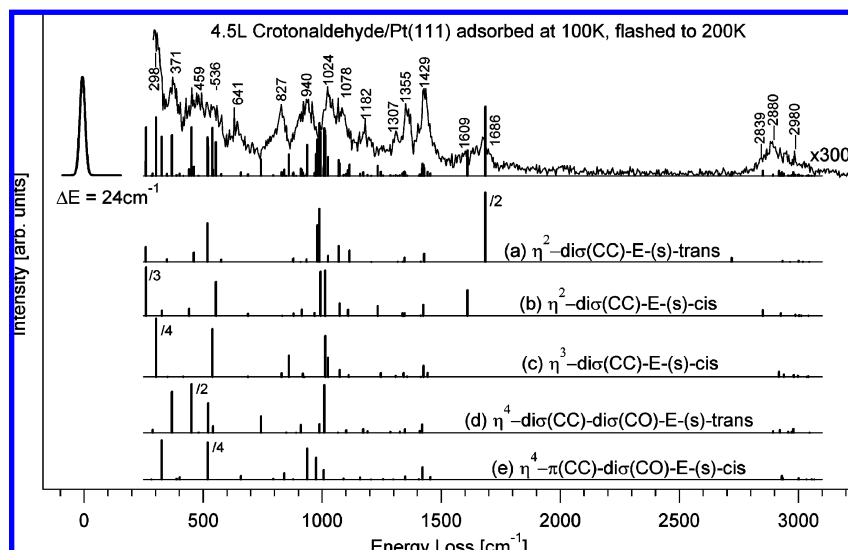


Figure 9. Analysis of the HREELS spectra of 4.5 L crotonaldehyde/Pt(111) after annealing to 200 K with the computed HREEL spectra of the five identified adsorption forms (at a theoretical coverage of 1/9 ML).

out-of-plane $\gamma(\text{CH})$ vibrations follow. The $\nu(\text{CC})$ stretching modes appear between the $\delta(\text{CH})$ and $\gamma(\text{CH})$ modes, and their actual positions depend strongly on the adsorption form.

Identification of the $\eta^3\text{-di}\sigma(\text{CC})\text{-}\sigma(\text{O})\text{-E(s)-cis}$ structure is more complicated as it shows only a small number of intense vibrational losses. Its presence is best seen with the experimental loss peaks at 827 and 303 cm^{-1} , which can be assigned with the computed $\gamma'(\text{CH}_3)$ vibration (860 cm^{-1}) and the dominant $\nu(\text{Pt-O})$ stretching mode of the η^3 form (320 cm^{-1}).

Finally, the identification of the η^4 structures in the mixed adsorbate phase requires the same strategy as they are also rather weak. The necessity of the $\eta^4\text{-E(s)-trans}$ structure is underlined by the experimental loss peak at 371 cm^{-1} and the band from 459 cm^{-1} to 536 cm^{-1} , which are interpreted by the symmetric molecule–substrate stretching mode $\nu_s(\text{PtC2-PtC3})$ computed at 369 cm^{-1} and the coupled $\nu_{\text{as}}(\text{PtO-PtC1})$ and $\delta(\text{C2=C3-C4})$ (452 cm^{-1}) normal modes. The $\eta^4\text{-E(s)-cis}$ adsorption complex gives a better understanding of the experimental loss signals at 641 and 940 cm^{-1} , which are assigned to the $\gamma_s(\text{C2H2-C3H3})$ mode calculated at 938 cm^{-1} with medium intensity and the backbone deformation vibration $\delta(\text{O=C1-C2})$ at 659 cm^{-1} with weak intensity. Its medium intense normal mode $\nu_{\text{as}}(\text{PtO + PtC1 - PtC2 + PtC3})$ computed at 325 cm^{-1} also contributes to the measured loss intensity at 298 cm^{-1} .

Although the systematic error arising from the computation of the frequencies at the harmonic level is very small in the region below 1500 cm^{-1} , significant deviations may arise due to the neglect of the coupling to phonons below $\sim 300 \text{ cm}^{-1}$. Test calculations, including systematically only the first layer of Pt atoms or the relaxed metal layers in the vibrational analysis, showed that the molecular and hindered vibrations below 150 cm^{-1} are mostly affected (shifts up to 50 cm^{-1}), while between 150 and 300 cm^{-1} , only small errors are found ($< 20 \text{ cm}^{-1}$). However, because of the coupling, the intensity of all signals is being dispersed.

In contrast to the calculated frequencies, the HREELS loss intensities differ sizably for several normal modes from the experimental data. Aside from the $\nu(\text{C1=O})$ vibrations of the two η^2 structures around $\sim 1686 \text{ cm}^{-1}$, mainly the intense out-of-plane normal modes $\gamma''(\text{CH}_3)$ of all adsorption forms (around 980 cm^{-1}) and the asymmetric stretching modes $\nu_{\text{as}}(\text{PtC2-PtC3})$ and $\nu_{\text{as}}(\text{PtC1-PtO})$ (both around 500 cm^{-1}) for $\text{di}\sigma$ -coordinated

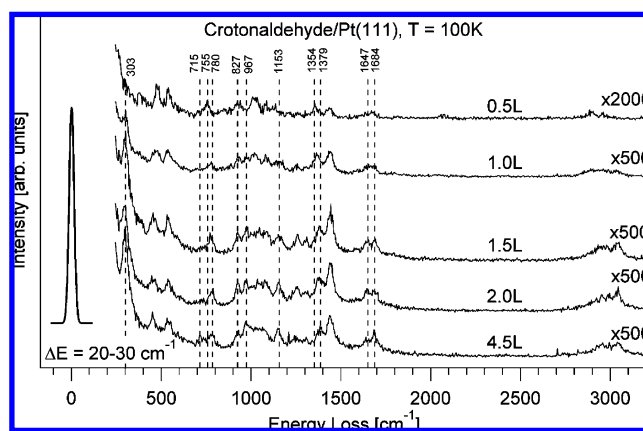


Figure 10. HREELS spectra of increasing exposures of crotonaldehyde dosed to the Pt(111) sample at 100 K (specular mode, 60° off normal, $E_0 = 4.7 \text{ eV}$).

entities have extraordinarily large intensities. This phenomenon has already been ascribed to the ideal periodicity in the theoretical models,^{15,24} while no ordered superstructure can be detected in LEED experiments. The lack of order and orientation of structures lead to frequency broadening and dispersion of the intensities of the experimental loss peaks. Also contributions from impact scattering are not included in our theoretical model but can be important for understanding the intensities of weaker modes. Furthermore, for the simplicity of the analysis, all structures are treated to be present in equal amounts.

The coverage dependence of the HREEL spectra recorded below 200 K shows, unlike for prenal on Pt(111), changes at very small exposures indicating a variation in the composition of the adsorbate phase (Figure 10). For very small exposures of crotonaldehyde on Pt(111), for which our TPD experiments did not show any desorption of intact aldehyde, the HREEL spectra are nearly identical to the ones recorded after annealing larger exposures to 200 K.

Small deviations are observed for the loss peaks at 1153, 967, 827, and 780 cm^{-1} , which appear damped significantly. The latter one even shifts to 755 cm^{-1} in the 0.5 L experiment. Simultaneously, the loss signal around 1379 cm^{-1} assigned to the $\delta''(\text{CH}_3)$ and $\nu(\text{CH}_3)$ vibrations also shifts to 1354 cm^{-1} in the submonolayer HREEL spectra, while the other loss signals,

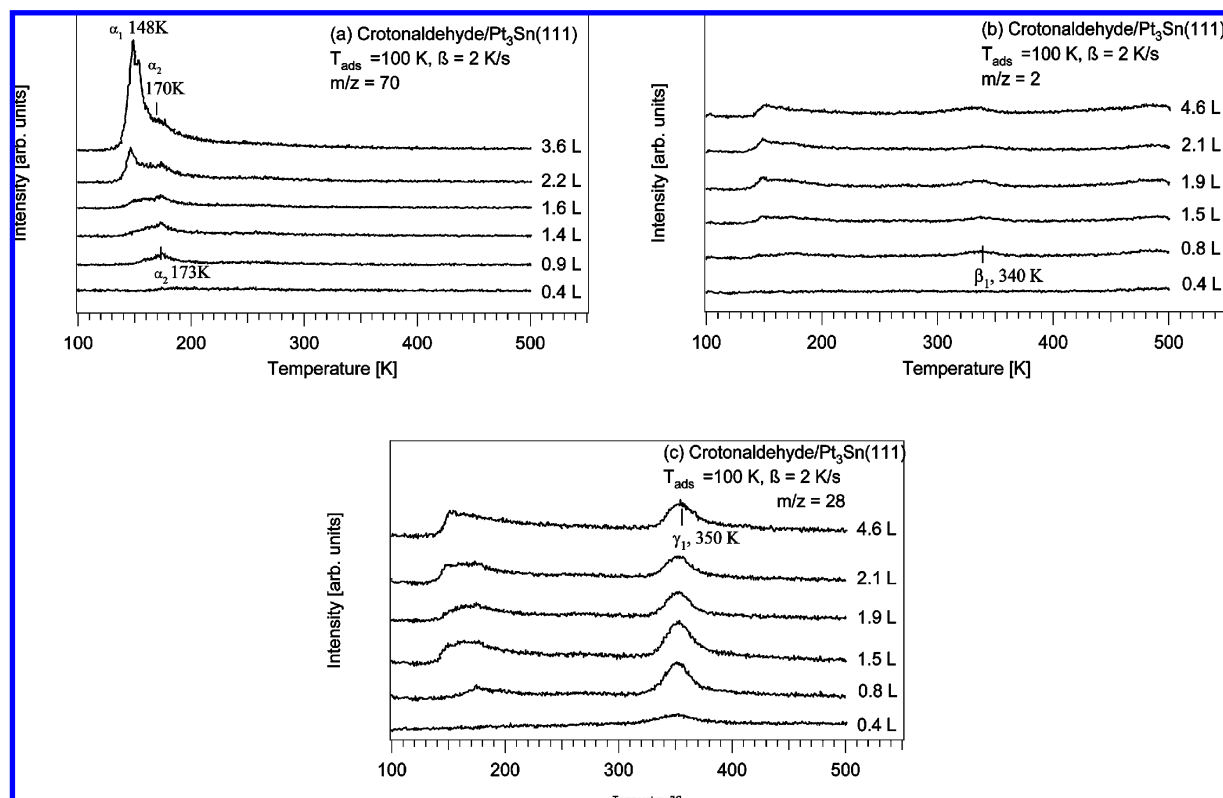


Figure 11. TPD spectra of crotonaldehyde/Pt₃Sn(111): (a) Crotonaldehyde desorption ($m/z = 70$) and the decomposition products (b) H₂ ($m/z = 2$) and (c) CO ($m/z = 28$).

for example, the $\nu(\text{CO})$ stretching mode $\sim 1684 \text{ cm}^{-1}$, seem to be unaffected. It can be seen from the evolution of the latter peak in the HREELS coverage series that it consists of a second component at roughly 1647 cm^{-1} .

Because DFT calculations performed at a higher theoretical coverage of $\Theta = 1/6 \text{ ML}$ did not produce any significant variations as compared to those at $1/9 \text{ ML}$, we expect that the changes in the experimental data are mainly due to population changes of the various structures. The submonolayer spectra at 100 K are matched best by choosing only three of the previously assigned structures: $\eta^2\text{-di}\sigma(\text{CC})\text{-E(s)-trans}$, $\eta^4\text{-}\pi(\text{CC})\text{-di}\sigma(\text{CO})\text{-E(s)-cis}$, and $\eta^4\text{-di}\sigma(\text{CC})\text{-di}\sigma(\text{CO})\text{-E(s)-trans}$ forms. The decrease of the intensity at 827 cm^{-1} points to a lower fraction of the $\eta^3\text{-di}\sigma(\text{CC})\text{-}\sigma(\text{O})\text{-E(s)-cis}$ structure, and the $\eta^2\text{-di}\sigma(\text{CC})\text{-E(s)-cis}$ structure also seems to be no longer important for analysis because the intensity measured around 1647 cm^{-1} is comparably small. Therefore, a trend to a preference of the flat η^4 coordination types of high hapticity can be inferred for low coverages. This trend is in line with previous results obtained on the system acrolein/Pt(111) by Loffreda et al.²⁵

4.3. Crotonaldehyde on the Pt₃Sn(111) and Pt₂Sn(111) Surface Alloys. **4.3.1. Chemisorbed States from TPD.** The TPD measurements performed for several exposures of crotonaldehyde on Pt₃Sn(111) surface alloys show qualitatively a similar behavior to Pt(111) (Figure 11). Here, too, the activation energy for intact desorption of the strongly bonded crotonaldehyde species appears to be larger than that for the barrier for their decomposition.

As evidenced by an overall decrease in the integral QMS intensities compared to Pt(111), the amount of chemisorbed crotonaldehyde is reduced by alloying. A low-temperature desorption state of intact crotonaldehyde is detected at $\sim 170 \text{ K}$ (α_2 , Figure 11c, $E_{\text{des}} = 36.9 \pm 1.5 \text{ kJ/mol}$ from Redhead analysis⁵⁰), while at ~ 340 and 350 K the desorption of H₂

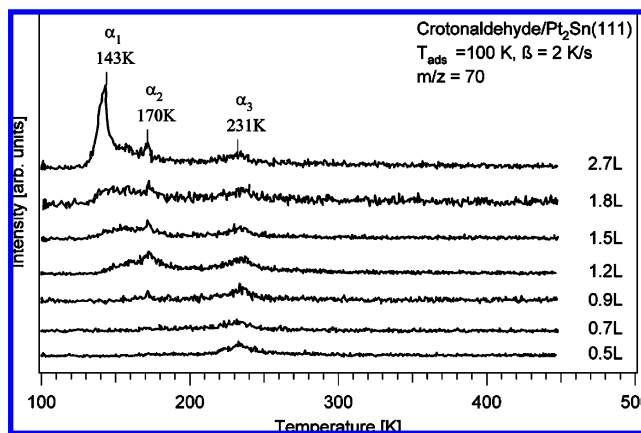


Figure 12. TPD spectra of crotonaldehyde adsorbed onto the Pt₂Sn/Pt(111) surface alloy.

(Figure 11b) and CO (Figure 11c), respectively, is measured even for low exposures. The molecular H₂ desorption, which is limited by recombination,¹⁹ is very weak and wide (about 40 K) in comparison to the signals observed on Pt(111). In contrast, the TPD spectra of CO (Figure 11c) present a well-defined desorption state around $350 \pm 5 \text{ K}$, which saturates for exposures above $\sim 0.8 \text{ L}$. Its desorption temperature is consistent with the one obtained for a saturation coverage of CO on a Pt₃Sn(111) surface alloy¹⁹ (353 K) but significantly lower than the CO desorption measured in the decomposition process of crotonaldehyde on Pt(111).

The desorption H₂ and CO again point to a decomposition of chemisorbed aldehyde species. This is indeed surprising as we expected from studies on cyclopentene,⁵² cyclohexene,⁵³ and prenal¹⁵ that Sn acts as an inhibitor for decomposition. Because the amount of desorbing CO varies, we conclude that the

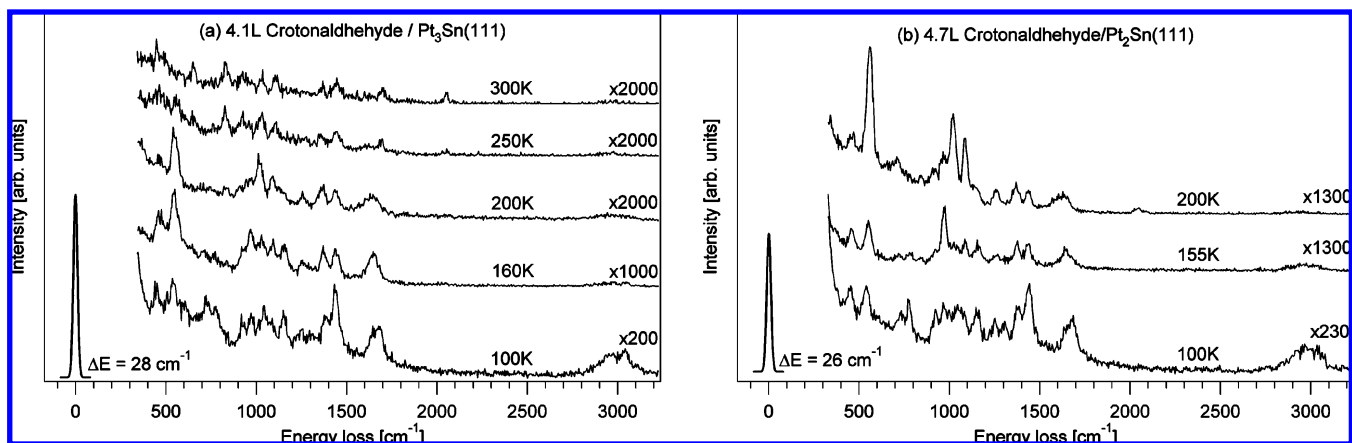


Figure 13. Experimental HREELS spectra recorded after different annealing steps of multilayer coverages of crotonaldehyde adsorbed at 100K onto the (a) $p(2 \times 2)$ -Pt₃Sn/Pt(111) and (b) $(\sqrt{3} \times \sqrt{3})R30^\circ$ -Pt₂Sn/Pt(111) surface alloys. Measurements have been performed in the dipolar regime ($E_0 = 4.7$ eV, incidence 60° angle off normal).

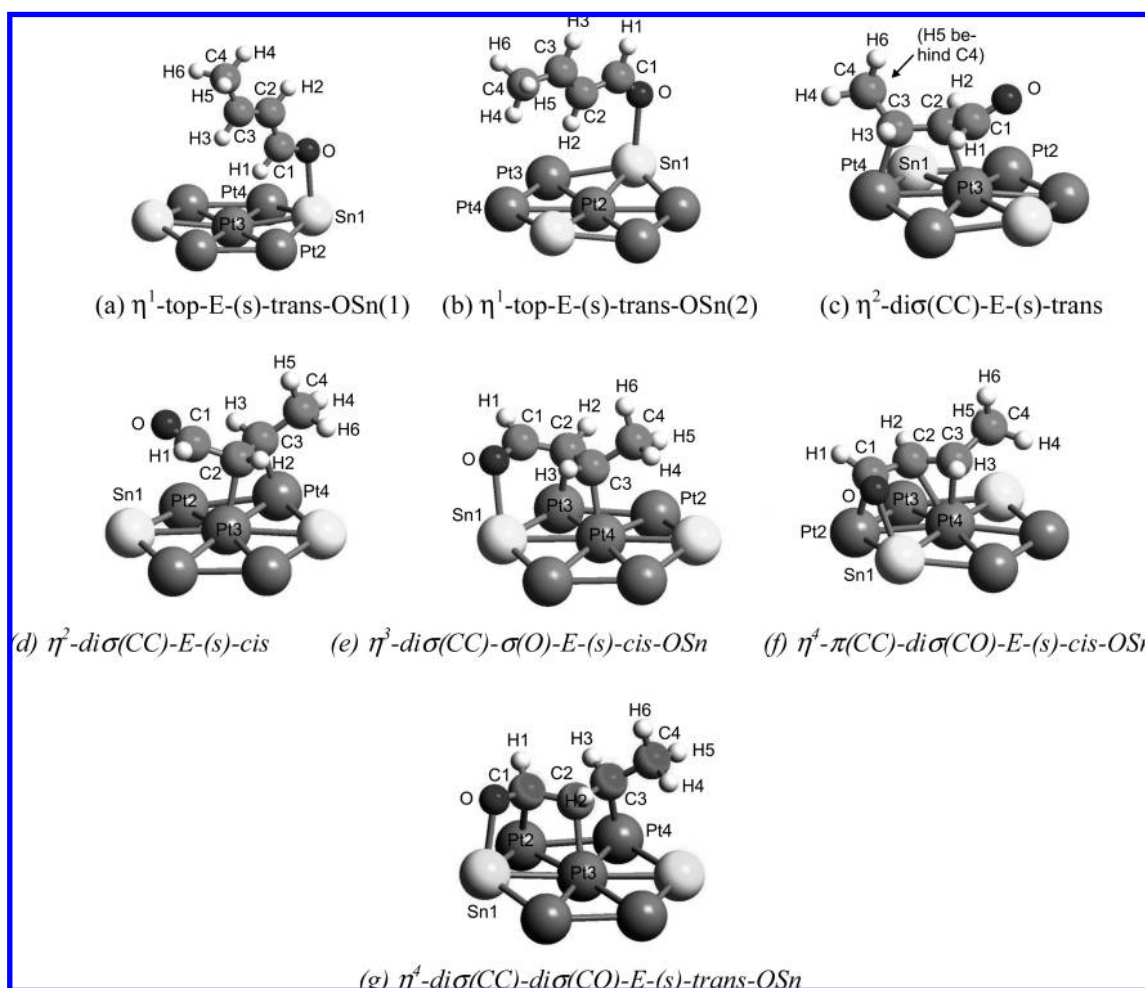


Figure 14. Optimized adsorption structures of crotonaldehyde on Pt₃Sn(111) ($\Theta_{\text{DFT}} = 1/12$ ML). Note that the aldehydic oxygen is always interacting with a Sn atom.

prepared Pt₃Sn(111) surfaces exhibit a non-negligible, varying density of defects such as remaining Pt(111) patches. However, as the LEED control experiments did not exhibit any significant variation of the superstructure spot widths, we cannot exclude that the decomposition might occur on the alloy itself. From a comparison of the integrated CO desorption peak areas on both model catalysts, we estimate that the amount of decomposition products desorbing from this surface alloy is as low as 50% of the amount undergoing decomposition on Pt(111). From Red-

head analysis⁵⁰ of CO desorption, an activation barrier of 91.5 ± 1.5 kJ/mol is obtained that represents an upper limit to the activation energy of the decomposition process. It is reduced by about 10% from the alloying value on Pt(111).

The TPD results of crotonaldehyde on the Pt₂Sn(111) surface alloy (Figure 12) support the trend of decreasing adsorption strength with increasing surface tin fraction; crotonaldehyde chemisorbs reversibly without undergoing decomposition at all. The monolayer desorption state at 231 K (α_3 , 59.6 ± 1.5 kJ/

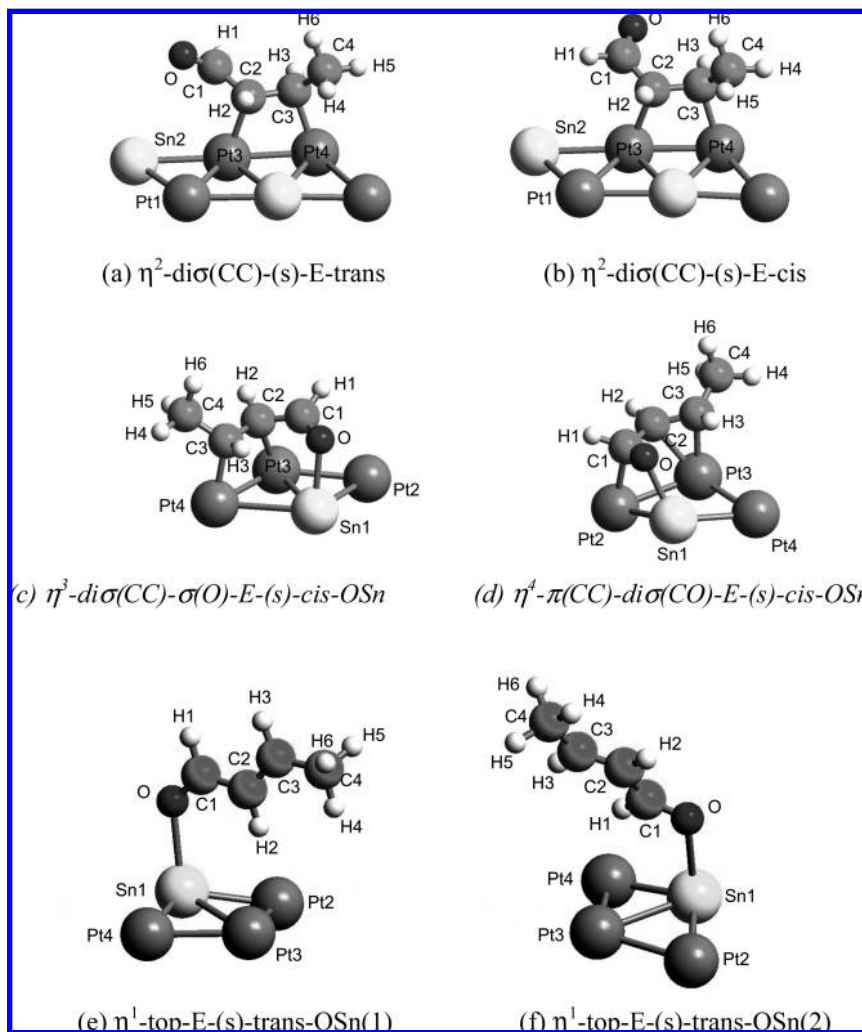


Figure 15. Optimized structures of the most stable configurations of crotonaldehyde on $\text{Pt}_2\text{Sn}(111)$: (a) and (b) from DFT optimizations at a theoretical coverage of 1/6 ML and (c–f) at $\Theta_{\text{DFT}} = 1/9$ ML.

mol) is found at somewhat higher temperatures compared to the desorption states of the intact aldehyde on $\text{Pt}(111)$ and $\text{Pt}_3\text{Sn}(111)$ (α_1 – α_3). Besides the multilayer desorption (about 143 K), one first-order low-temperature desorption peak is detected at 170 K (44.4 ± 1.5 kJ/mol).

4.3.2. HREELS Results of Crotonaldehyde on the $\text{Pt}_n\text{Sn}(111)$ Surface Alloys. Similar to $\text{Pt}(111)$, exposure and temperature-dependent HREELS experiments have been performed on the $\text{Pt}_3\text{Sn}(111)$ and $\text{Pt}_2\text{Sn}(111)$ surface alloys. Consistent with the intensity decreases measured in the TPD experiments, much weaker loss intensities are found on these surface alloys.

In Figure 13a, a HREELS series recorded on a $\text{Pt}_3\text{Sn}/\text{Pt}(111)$ surface alloy shows the transition from a multilayer spectrum (100 K) to different low-temperature adsorbate phases, which are observed after annealing to 160 and 200 K, respectively. Going to higher temperatures, the HREEL spectra strongly change again. These spectra resemble those recorded above 300 K on $\text{Pt}(111)$, yet the peak positions are different. Notably, the evolution of CO bonded on Pt top sites (peak at 2054 cm^{-1}) is similar to the behavior of crotonaldehyde on $\text{Pt}(111)$ and indicates decomposition. Because of intermolecular interactions, the position of this $\nu(\text{CO})$ vibration is shifted from its position at 2090 cm^{-1} in a saturated monolayer of CO on $\text{Pt}_3\text{Sn}/\text{Pt}(111)$.¹⁹

HREELS measurements on the $\text{Pt}_2\text{Sn}/\text{Pt}(111)$ surface alloy (Figure 13b) show again a typical multilayer spectrum upon adsorption at 100 K. After annealing to 155 K in order to remove

the physisorbed crotonaldehyde, a HREEL spectrum of reversibly chemisorbed crotonaldehyde is recorded, which differs significantly from the ones found on $\text{Pt}(111)$ and $\text{Pt}_3\text{Sn}/\text{Pt}(111)$. Upon annealing to 200 K, further changes of the vibrational fingerprint lead to a spectrum, which resembles the one recorded on $\text{Pt}_3\text{Sn}/\text{Pt}(111)$. In agreement with the TPD results, only very weak and broad traces of hydrocarbon residues are detected for higher annealing temperatures.

The DFT calculations of crotonaldehyde on the surface alloys have been performed for a low coverage of 1/12 ML on $\text{Pt}_3\text{Sn}/\text{Pt}(111)$ and (1/9 ML) on $\text{Pt}_2\text{Sn}/\text{Pt}(111)$ as well as a high-coverage 3×2 supercell on $\text{Pt}_2\text{Sn}/\text{Pt}(111)$ (1/6 ML). After optimizing the geometries of a large number of configurations on the surface alloys, we have characterized the vibrational properties of all the stable adsorption forms. While in their previous total energy calculations Delbecq et al.²³ have considered only crotonaldehyde adsorption on Pt_2Sn with a small number of structures, we have modeled all conceivable forms, including those with C–Sn interactions. However, these C–Sn bonds are unstable on both Pt–Sn alloys. Bonds from the aldehydic oxygen to Pt atoms are much weaker than O–Sn interactions but are stable in a few η^3 and η^4 configurations ($E_{\text{ads}} > -25$ kJ/mol). Yet, they alone are not sufficient to stabilize an adsorption complex.

From the optimizations on $\text{Pt}_3\text{Sn}/\text{Pt}(111)$ (61 initial geometries considered), 23 stable configurations are obtained that can again

Downloaded by UNIWERSYTET WROCLAWSKI on August 19, 2009
Published on July 2, 2009 on http://pubs.acs.org | doi: 10.1021/jp903473m

TABLE 6: Adsorption Energies and Main Bond Distances of the Adsorption Structures of Crotonaldehyde on Pt₃Sn(111)

Pt ₃ Sn(111)							
geometry	η^1 -top- <i>E</i> -(s)- <i>trans</i> -OSn(1)	η^1 -top- <i>E</i> -(s)- <i>trans</i> -OSn(2)	η^2 -di σ (CC)- <i>E</i> -(s)- <i>trans</i>	η^2 -di σ (CC)- <i>E</i> -(s)- <i>cis</i>	η^3 -di σ (CC)- σ (O)- <i>E</i> -(s)- <i>cis</i> -OSn	η^4 - π (CC)-di σ (CO)- <i>E</i> -(s)- <i>cis</i> -OSn	η^4 - π (CC)-di σ (CO)- <i>E</i> -(s)- <i>cis</i> -OSn
supercell	$2\sqrt{3} \times 2\sqrt{3}$	$2\sqrt{3} \times 2\sqrt{3}$	$2\sqrt{3} \times 2\sqrt{3}$	$2\sqrt{3} \times 2\sqrt{3}$	$2\sqrt{3} \times 2\sqrt{3}$	$2\sqrt{3} \times 2\sqrt{3}$	$2\sqrt{3} \times 2\sqrt{3}$
E_{ads} (kJ/mol)	-33.2	-30.8	-32.9	-34.0	-51.2	-41.7	-41.7
r(O-C1) (Å)	1.24	1.24	1.23	1.23	1.27	1.34	1.34
r(C1-C2) (Å)	1.44	1.44	1.49	1.48	1.44	1.47	1.47
r(C2-C3) (Å)	1.35	1.35	1.50	1.49	1.49	1.42	1.42
r(C3-C4) (Å)	1.48	1.48	1.52	1.52	1.52	1.50	1.50
r(O-M) (Å)	2.49	2.54	-	-	2.37	2.20	2.20
r(C1-M) (Å)	-	-	-	-	-	2.23	2.23
r(C2-M) (Å)	-	-	2.16	2.17	2.23	2.31	2.31
r(C3-M) (Å)	-	-	2.15	2.15	2.14	2.21	2.21

TABLE 7: Adsorption Energies and Main Bond Distances of the Adsorption Structures of Crotonaldehyde on Pt₂Sn(111)

Pt ₂ Sn(111)						
geometry	η^2 -di σ (CC)- <i>E</i> -(s)- <i>trans</i>	η^2 -di σ (CC)- <i>E</i> -(s)- <i>cis</i>	η^3 -di σ (CC)- σ (O)- <i>E</i> -(s)- <i>cis</i> -OSn	η^4 - π (CC)-di σ (CO)- <i>E</i> -(s)- <i>cis</i> -OSn	η^1 -top- <i>E</i> -(s)- <i>trans</i> -OSn(1)	η^1 -top- <i>E</i> -(s)- <i>trans</i> -OSn(2)
supercell	3 × 2	3 × 2	3 × 3	3 × 2	3 × 3	3 × 3
E_{ads} (kJ/mol)	−19.7	−29.5	−49.1	−16.4	−29.0	−28.2
r(O−C1) (Å)	1.23	1.23	1.28	1.34	1.34	1.24
r(C1−C2)(Å)	1.48	1.48	1.44	1.47	1.47	1.45
r(C2−C3)(Å)	1.50	1.50	1.49	1.42	1.42	1.35
r(C3−C4)(Å)	1.52	1.52	1.52	1.51	1.51	1.48
r(O−M) (Å)	—	—	2.34	2.16	2.27	2.57
r(C1−M) (Å)	—	—	—	2.25	2.24	—
r(C2−M) (Å)	2.16	2.17	2.25	2.32	2.27	—
r(C3−M) (Å)	2.14	2.13	2.13	2.20	2.19	—

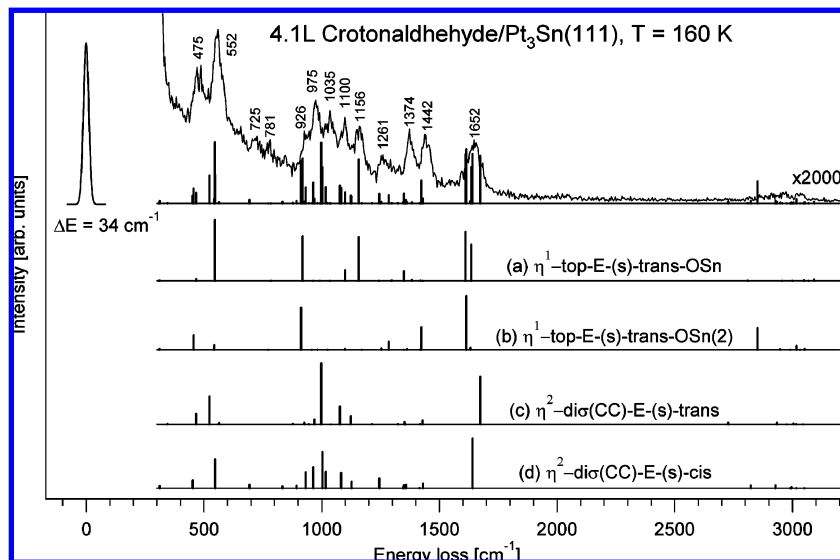


Figure 16. Comparison of the HREELS spectrum recorded after annealing 4.1 L of crotonaldehyde adsorbed at 100 K onto the $p(2 \times 2)$ -Pt₃Sn/Pt(111) surface alloy to 160 K with the theoretical spectra of the identified η^1 -top-OSn and η^2 -di σ (CC) adsorption structures ($\Theta_{\text{DFT}} = 1/12$ ML).

be grouped into 8 strongly ($-51.2 < E_{\text{ads}} < -30$ kJ/mol) and 15 weakly bonded forms ($E_{\text{ads}} > -30$ kJ/mol). Unlike on Pt(111), the stronger bonded structures include not only flat η^2 -di σ (CC), η^3 , and η^4 configurations but also two vertical η^1 -top-*E(s)-trans*-OSn geometries ($E_{\text{ads}} = -33.2$ and -30.8 kJ/mol). Figure 14 presents the configurations that have been identified on Pt₃Sn(111).

Even for the most stable η^3 -di σ (CC)- σ (O)-*E(s)-cis*-OSn (-51.2), η^4 - π (CC)-di σ (CO)-*E(s)-cis*-OSn (-41.7), η^4 -di σ (CC)-di σ (CO)-*E(s)-trans*-OSn (-37.9), η^2 -di σ (CC)-*E(s)-trans* (-32.9), and η^2 -di σ (CC)-*E(s)-cis* forms (-34.0 kJ/mol), we find a sizable decrease of the adsorption energies by about 40% compared to those of Pt(111).

For the low-coverage (1/9 ML) crotonaldehyde/Pt₃Sn/Pt(111) supercell, the most important results have already been discussed in ref 24. Here, from an even larger set of more than 64 initial structures, only 14 structures turned out to be stable. Out of these, seven exhibited weak adsorption energies (above -25 kJ/mol), and seven structures turned out to be more significantly bonded (below -28 kJ/mol). Among the most competitive forms, five could be assigned to the low-coverage/high-temperature phase recorded with HREELS after annealing to 200 K: η^2 -di σ (CC)-*E(s)-trans* (-33.7), η^3 -di σ (CC)- σ (O)-*E(s)-cis*-OSn (-49.1), η^4 - π (CC)-di σ (CO)-*E(s)-cis*-OSn (-29.0), η^1 -top-*E(s)-trans*-OSn(1) (-28.2), and η^1 -top-*E(s)-trans*-OSn(2) (-22.5) (Figure 15). Hence, compared to Pt(111), the adsorption energies of crotonaldehyde on Pt₃Sn/Pt(111) decrease generally by $\sim 50\%$ for the most stable forms (by ~ 30 – 40 kJ/mol).

The calculations of the high-coverage situation on Pt₃Sn(111) (1/6 ML) have been performed for only four of the most stable structures plus an additional representative for each of the other coordination types. As expected, the increase in coverage leads to a sizable weakening of the adsorption energies, but the same coordination types remain competitive: η^2 -di σ (CC)-*E(s)-trans* (-19.7) and η^2 -di σ (CC)-*E(s)-cis* forms (-29.5 kJ/mol) and η^4 - π (CC)-di σ (CO)-*E(s)-cis*-OSn (-16.4). Furthermore, the increase in the coverage causes a transformation of the η^3 -di σ (CC)- σ (O)-*E(s)-cis*-OSn structure to a more vertical metallacycle that only adsorbs via the oxygen and the β -carbon, i.e., the η^2 -di σ (C3,O)-*E(s)-cis*-OSn (-27.1) form, which has not been found previously. Obviously, the lateral interaction prevents a flat orientation in this case.

Surprisingly, in the context of the general destabilization induced by the alloying, neither the optimized geometries (Tables 6 and 7) of the surface structures nor their vibrational properties differ significantly from the values of the corresponding forms on Pt(111). This contrasts with the strong decreases in the adsorption energies.

All bond lengths of the molecular backbones typically reveal elongations well below 0.02 Å from the corresponding values on Pt(111). The molecule–surface bonds are more strongly affected, especially those to the aldehydic C1=O moiety, which show increases of 0.08 to 0.12 Å for the η^3 and η^4 forms. The Pt–C bonds of the vinylic C2=C3 part of all structures remain very similar to those on Pt(111) (increases < 0.02 – 0.04 Å), indicating only a weak influence of Sn on the bond strengths. Because the bonding metal atom is changed to Sn on the surface alloys, which protrudes slightly from the surface planes,²³ the larger effects on the bonds from the aldehydic function are not very surprising. Importantly, the optimized structures of a given coordination type are extremely similar on both surface alloys. Their bond distances, rather independent from the coverage as evidenced by the calculations on Pt₂Sn, deviate by less than ± 0.01 Å on both surface alloys and their molecule–surface bonds agree within ± 0.02 Å (with the exception of the top OSn forms, where the O–Sn bond length is significantly longer on Pt₂Sn).

The small influence of alloying on the structures of the bonds is also reflected by the vibrational fingerprints. From the comparison of the computed HREEL spectra of related configurations on Pt(111) and both surface alloys, it is seen that Sn induces only small perturbations on the frequencies and intensities of vibrations lying above ~ 300 cm⁻¹, in particular, also for the ν (CC) and ν (CO) modes ($\Delta\nu < \sim 20$ cm⁻¹). Hence, the modes in this fingerprint region are primarily suitable for identifying certain coordination types and isomers rather than for characterizing the alloying effects.

Furthermore, we find only slight redshifts for the normal modes associated with the molecule–substrate stretching modes and hindered modes below ~ 300 cm⁻¹. Although this is qualitatively in agreement with the decrease in the adsorption energies, these redshifts [by ~ 15 cm⁻¹ going from Pt(111) to Pt₃Sn and also to Pt₂Sn] appear too small to account for the considerable weakening of the adsorption energies.

TABLE 8: Computed Frequencies of Important Vibrational Normal Modes of Crotonaldehyde Adsorption Structures on Pt₃Sn(111), $\Theta = 1/12$ ML

geometry	Pt ₃ Sn(111)						
	η^1 -top- <i>E</i> -(<i>s</i>)- <i>trans</i> -OSn(2)	η^2 - $\text{di}\sigma(\text{CC})$ - <i>E</i> -(<i>s</i>)- <i>trans</i>	η^2 - $\text{di}\sigma(\text{CC})$ - <i>E</i> -(<i>s</i>)- <i>cis</i>	η^3 - $\text{di}\sigma(\text{CC})$ - $\sigma(\text{O})$ - <i>E</i> -(<i>s</i>)- <i>cis</i> -OSn	η^4 - $\pi(\text{CC})$ - $\text{di}\sigma(\text{CO})$ - <i>E</i> -(<i>s</i>)- <i>cis</i> -OSn		
supercell	$2\sqrt{3} \times 2\sqrt{3}$	$2\sqrt{3} \times 2\sqrt{3}$	$2\sqrt{3} \times 2\sqrt{3}$	$2\sqrt{3} \times 2\sqrt{3}$	$2\sqrt{3} \times 2\sqrt{3}$	$2\sqrt{3} \times 2\sqrt{3}$	
$\nu(\text{C}-\text{H})$ range	3092–2810	3045–2728	3051–2824	3054–2930	3067–2936	3067–2936	
$\nu(\text{C}1=\text{O})$	1611	1674	1641	1460	1166	1166	
$\nu(\text{C}1-\text{C}2)$	1157	1039	1003	1036	978	978	
$\nu(\text{C}2=\text{C}3)$	1635	1124	1128	1124	1454	1454	
$\nu(\text{C}3-\text{C}4)$	1101	1077	1083	1087	1092	1092	
$\nu_{\text{as}}(\text{PtC}2-\text{PtC}3)^a$	—	524	548	533	515	515	
$\nu_s(\text{PtC}2-\text{PtC}3)^a$	—	345	452	335	397	397	
$\nu_s(\text{M}-\text{O})^b$	127	—	—	316	—	—	
$\nu_{\text{as}}(\text{MO}-\text{PtCl})^a$	—	—	—	—	302	302	
$\nu_s(\text{MO}-\text{PtCl})^a$	—	—	—	—	234	234	

^aThese normal modes show complex couplings to other vibrations, which are omitted here for the sake of clarity. ^bThis normal mode is only present for η^1 and η^3 forms.

In general, the changes in the geometries and vibrational spectra indicate that the weakening of the adsorption is mainly caused by electronic effects, whereas geometric effects, resulting mainly from the buckling of the Sn atoms, are less important.

From the dependence of the experimental HREEL spectra on temperature and coverage (Figure 13), we expect phase transitions from high- to low-coverage phases on both surface alloys. This is also consistent with the low-temperature desorption states from TPD (Figures 11a and 12, trace $m/z = 70$) because these phase transitions are accompanied by partial desorption processes.

Although another possible reason for the observed changes in the HREEL spectra might be frequency shifts and intensity variations arising from changes in the intermolecular interactions due to a coverage decrease, we can rule out this option from DFT. As on pure Pt(111), the vibrational analysis carried out for low- (1/6 ML) and high-coverage (1/9 ML) supercells on the Pt₃Sn surface alloy did not show any significant changes of the fingerprints ($\Delta\nu < 20 \text{ cm}^{-1}$) for the corresponding stable adsorption structures. This seems to be a common phenomenon for prenal and crotonaldehyde on Pt(111), Pt₃Sn(111), and Pt₂Sn(111) in the coverage regime from 1/6 to 1/12 ML. However, because the relative stabilities of the various adsorption forms are strongly affected, the DFT results support transitions between mixed phases of different competitive configurations.

The analysis of the experimental HREEL spectrum of the low-temperature adsorbate phase on Pt₃Sn(111) (160 K, Figure 16) with the computed spectra of the structures from DFT leads to the conclusion that the adsorbed layer is composed of four components, two of which are predominant. While the η^2 - $\text{di}\sigma(\text{CC})$ -*E*-(*s*)-*trans* and η^2 - $\text{di}\sigma(\text{CC})$ - $\sigma(\text{O})$ -*E*-(*s*)-*cis* adsorption geometries account for most of the observed loss peaks, also a small fraction of two η^1 -top-*E*-(*s*)-*trans*-OSn forms is required to explain the experimental data satisfactorily (important normal modes are summarized in Table 8).

The presence of η^2 - $\text{di}\sigma(\text{CC})$ -coordinated species is evidenced in particular by the experimental signals at 1652 and 975 cm^{-1} , which are assigned to the $\nu(\text{C}1=\text{O})$ vibrations and coupled γ deformation modes of the *E*-(*s*)-*trans* (DFT, 1674; 970 cm^{-1}) and *E*-(*s*)-*cis* rotational isomers (DFT, 1641; 965 cm^{-1}). The set of out-of-plane γ deformation modes of the vinylic, aldehydic, and methyl hydrogens leads to the measured peaks around 975 and 926 cm^{-1} . In fact the intensity of the first signal can be understood from the theoretical analysis, but the second peak seems too intense to result only from these η^2 structures.

At 1261 cm^{-1} , a signal is measured which gains a fraction of its intensity from the asymmetrically coupled $\delta_{\text{as}}(\text{C}2\text{H}2-\text{C}3\text{H}3)$ vibrations (DFT, 1245 cm^{-1}). Because here also the recorded intensity extending to higher wavenumbers cannot be accounted for by the η^2 - $\text{di}\sigma(\text{CC})$ forms alone, the presence of additional surface complexes becomes obvious.

Similarly the intensity discrepancies between the experiments and computed HREEL spectra are found for the loss peak at 1156 cm^{-1} , which agrees with the $\nu(\text{C}2=\text{C}3)$ stretching modes computed at 1124 cm^{-1} and at 1128 cm^{-1} for the *E*-(*s*)-*trans* and *E*-(*s*)-*cis* isomers, respectively. However their intensity is quite weak.

The $\nu(\text{C}3-\text{C}4)$ vibrations of the methyl substituents are detected around 1100 cm^{-1} with somewhat larger intensity. They are computed at 1077 and 1083 cm^{-1} for the two η^2 structures. In contrast, the $\nu(\text{C}1-\text{C}2)$ modes are only active for the η^2 - $\text{di}\sigma(\text{CC})$ -*E*-(*s*)-*cis* structure (DFT, 1003 cm^{-1}), which therefore mainly accounts for the signal recorded at 1035 cm^{-1} , whereas

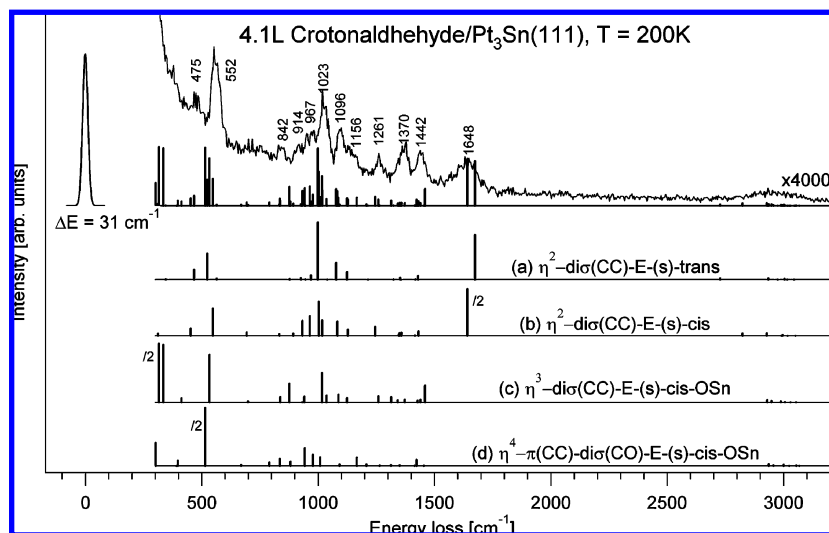


Figure 17. Comparison of the theoretical spectra of the identified η^2 , η^3 , and η^4 configurations ($\Theta_{\text{DFT}} = 1/12$ ML) with the experimental HREEL spectrum recorded of 4.1 L of crotonaldehyde annealed to 200 K on the $p(2 \times 2)$ -Pt₃Sn/Pt(111) surface alloy.

the corresponding mode of the $E(s)$ -*trans* structure computed at 1039 cm^{-1} is inactive.

Characteristic and dominant in the lower frequency region are the loss signals at 552 and 475 cm^{-1} . They can also be traced back specifically to the η^2 - $\text{di}\sigma(\text{CC})$ -coordinated species. For the leading contributions of the normal modes assigned to these loss peaks, namely, the $\nu_{\text{as}}(\text{PtC2-PtC3})$ vibration of the $E(s)$ -*trans* complex computed at 524 cm^{-1} and the $\nu_{\text{as}}(\text{PtC2-PtC3})$ mode (548 cm^{-1}) of the $E(s)$ -*cis* form, the destabilization of the adsorption energies does not manifest itself in significant shifts. Finally, an intense and broad peak measured around 256 cm^{-1} is assigned to a combination of the $\delta(\text{C1-C2=C3})$ deformation and the $\tau(\text{C1-C2})$ torsion vibration of the molecular backbone of the $E(s)$ -*cis* structure (DFT, 253 cm^{-1} , intense); the $E(s)$ -*trans* form does not exhibit any similar loss signal here.

Thus, only the loss peaks at 1652 , 1374 , 1156 , and 926 cm^{-1} remain explained unsatisfactorily by the two η^2 - $\text{di}\sigma(\text{CC})$ structures. From the theoretical HREEL spectra, it is however evident that the structures of higher hapticity, especially the η^3 configurations representing the most stable structures at a coverage of $1/12$ ML, are not compatible with the experiment at 160 K . Because the vertical adsorption complexes of the η^1 -top- $E(s)$ -*trans*-OSn coordination type show not only very good agreement with the overall fingerprint discussed so far but also allow for understanding of the missing intensities in the problematic cases, they are concluded to contribute to the HREEL spectrum recorded at 160 K .

Computed at 256 and 238 cm^{-1} , the $\delta(\text{C1-C2=C3})$ normal modes of the two η^1 -top- $E(s)$ -*trans*-OSn structures amplify the large intensity already obtained from η^2 - $\text{di}\sigma(\text{CC})$ - $E(s)$ -*cis* and help to explain the unusual width of the band detected at 256 cm^{-1} .

Furthermore, both η^1 forms contribute to the shoulder at 926 cm^{-1} with their $\gamma'(\text{CH}_3)$ vibrations that are calculated with medium loss intensity at 919 and 912 cm^{-1} . Another clear indicator of the presence of the more vertically oriented η^1 -top- $E(s)$ -*trans*-OSn adsorption complex is given by the experimental loss peak at 1156 cm^{-1} , which coincides with the computed $\nu(\text{C1-C2})$ stretching mode at 1157 cm^{-1} . Without inclusion of this η^1 complex, this signal is barely explainable.

Also, in the intermediate frequency region between 1200 and 1450 cm^{-1} , the η^1 geometries improve the analysis. Especially,

the loss signals detected at 1374 and 1442 cm^{-1} can now be explained by the multitude of $\nu(\text{CH}_3)$ and $\delta(\text{CH}_3)$ deformation modes of the η^1 and η^2 modes, which taken isolated would be too weak.

In the characteristic double-bond stretching region, the $\nu(\text{C2=C3})$ and the $\nu(\text{C1=O})$ stretching frequencies uncover another surprising result. For both η^1 adsorption geometries, the $\nu(\text{C1=O})$ vibrations are obtained essentially at identical values of 1611 and 1615 cm^{-1} ; likewise, the $\nu(\text{C2=C3})$ modes nearly coincide at 1635 and 1632 cm^{-1} . The computed normal modes thus agree well with the loss at 1652 cm^{-1} , which exhibits the width of the corresponding signal at 200 K on Pt(111) but is evidently more intense and defined. Although the width was explained previously on Pt(111) as a consequence of the disordering and random orientation, here it may in addition be understood simply from the variety of vibrations of the η^2 and η^1 that are assigned within this frequency window. Only the increased intensity is very different from Pt(111) and must be due to the new η^1 structures.

Therefore, considering the η^1 -top-OSn geometries together with the η^2 - $\text{di}\sigma(\text{CC})$ forms present on the surface, the experimental HREEL spectra can be understood well.

Annealing to 200 K changes the overall shape of the HREEL spectrum dramatically. The measured loss peaks at 475 , 914 , 967 , and 1156 cm^{-1} are damped strongly in contrast to the signals at 552 and 1023 cm^{-1} , which are now dominating the fingerprint region. In a comparable low-coverage HREEL spectrum recorded for 0.6 L crotonaldehyde/Pt₃Sn after annealing to 200 K , the latter signals are even more intense.

In combination with the assignments from the previous discussion, the weakening of the bands at 926 , 975 , (967 cm^{-1} at 200 K), and 1156 cm^{-1} as well as the damping at 1370 cm^{-1} (1374) and 1442 cm^{-1} (1442) show that the η^1 -top- $E(s)$ -*trans*-OSn surface species is no longer present at 200 K .

However, new signals of a η^3 - $\text{di}\sigma(\text{CC})$ - $\alpha(\text{O})$ - $E(s)$ -*cis* structure (Table 7) are observed in the HREELS experiments. The huge increase of the loss intensity at 1023 cm^{-1} is assigned to its methyl scissoring vibration $\gamma''(\text{CH}_3)$ computed at 1017 cm^{-1} . Besides that, particularly the intense $\nu(\text{C1-C2})$ mode of the η^2 - $E(s)$ -*cis* complex (1003 cm^{-1}) and the $\gamma''(\text{CH}_3)$ vibration of the corresponding $E(s)$ -*trans* form (999 cm^{-1}) account for the intensity increase here. Around 1261 and 1442 cm^{-1} , further contributions of the η^3 - $E(s)$ -*cis* structure improve the match

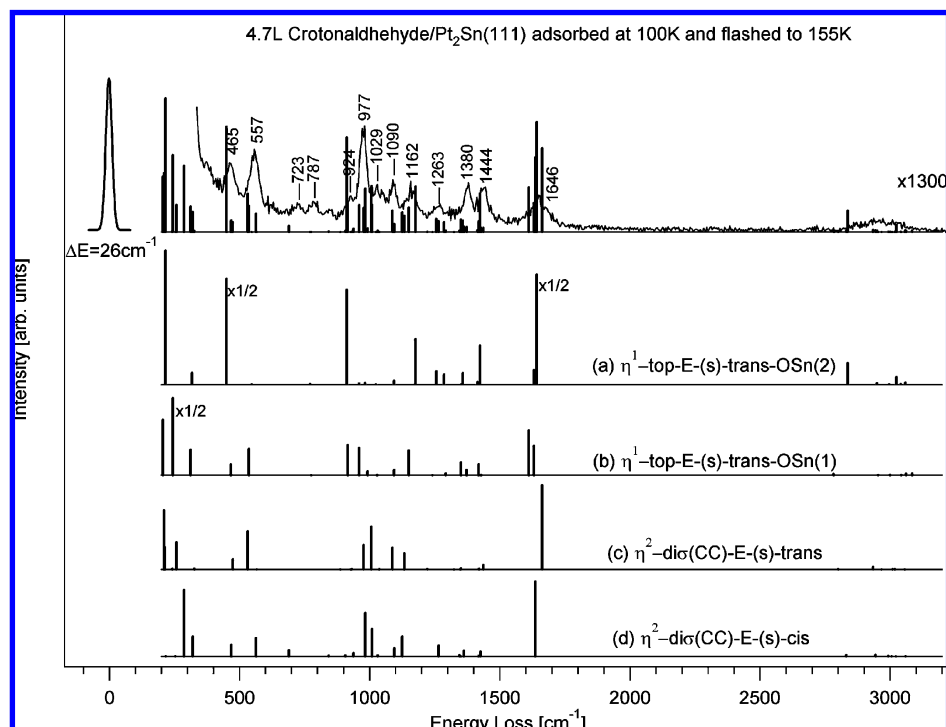


Figure 18. Analysis of the HREELS data of the crotonaldehyde monolayer (4.7 L) on $(\sqrt{3} \times \sqrt{3})R30^\circ$ -Pt₂Sn/Pt(111) at low temperatures (155 K) using the computed vibrational spectra of the η^1 -top-OSn and η^2 -di σ (CC) forms at coverages 1/9 ML and 1/6 ML, respectively.

with the experimental data. In detail, these are the $\delta_{\text{as}}(\text{C}_2\text{H}_2-\text{C}_3\text{H}_3)$ and the important $\nu(\text{C}=\text{O})$ normal modes computed with medium intensities at 1259 and 1460 cm^{-1} , respectively. Additional traces of the η^3 -di σ (CC)- $\sigma(\text{O})$ - $E(s)$ - cis surface species are attributed to the peaks at 842 cm^{-1} [$\gamma'(\text{CH}_3)$, 877 cm^{-1}] and at 552 cm^{-1} [$\nu_{\text{as}}(\text{PtC}_2-\text{PtC}_3)$, 533 cm^{-1}]. Especially the latter peak, which loses its contribution of the η^1 -top- $E(s)$ - $trans$ -OSn structure, remains dominant at 200 K. Finally the $\nu_s(\text{PtC}_2-\text{PtC}_3)$ and $\nu(\text{Pt}-\text{O})$ molecule-surface stretching modes are computed at 335 and 316 cm^{-1} , respectively, with large intensities, but they seem to be hidden in the high loss intensity of the η^2 forms, which give rise to the signal detected at 259 cm^{-1} .

Thus far, the computed HREEL spectra of the η^3 -di σ (CC)- $\sigma(\text{O})$ - $E(s)$ - cis -OSn, η^2 -di σ (CC)- $E(s)$ - $trans$, and η^2 -di σ (CC)- $E(s)$ - cis adsorption structures explain the experimental data quite well. Therefore, the transformation of the HREEL spectra between 160 and 200 K is interpreted as a surface reordering process that converts the low hapticity η^1 and η^2 coordination types to flat η^3 -di σ (CC) geometries.

However, another coordination type of the $E(s)$ - cis rotational isomer is found to be hardly distinguishable on energetic or spectroscopic grounds from the already identified ones; unlike the η^4 structures of the $E(s)$ - $trans$ or $Z(s)$ - $trans$ isomers, which can be excluded easily because of a number of mismatches of computed intense loss peaks in experimentally empty regions. Most of the detectable vibrational signals of the η^4 - π (CC)-di σ (CO)- $E(s)$ - cis -OSn (Table 8) complex happen to coincide with loss peaks already assigned previously. They are mostly very weak and thus difficult to detect.

On the Pt₂Sn surface alloy, crotonaldehyde behaves similarly as on Pt₃Sn. The experimental HREELS spectra of the low-temperature/high-coverage-mixed adsorbate phase recorded after adsorption at 100 K and annealing to 155 K are presented in Figure 18. Consistent with the relative stabilities at the theoretical coverages of 1/6 and 1/9 ML, it can be related to the η^2 -

di σ (CC)- $E(s)$ - $trans$, η^2 -di σ (CC)- $E(s)$ - cis , and η^1 -top- $E(s)$ - $trans$ -OSn structures (Table 9; for the top forms only, the coverage 1/9 ML is given for the sake of simplicity). On Pt₂Sn, the energy difference between the η^1 -top (−28.2 kJ/mol) and η^2 -di σ (CC) (−33.7 kJ/mol) structures is slightly more in favor of the latter as compared to that of Pt₃Sn (−33.2 and −34.0 kJ/mol, respectively).

The HREEL spectra after annealing to 155 K (Figure 18) show a strong increase in the intensity of the peak at 977 cm^{-1} as a major change in comparison with those taken on Pt₃Sn at 160 K (Figure 16). Consistent with the higher relative stabilities of the η^2 -di σ (CC) forms, it can be explained by the intense $\gamma(\text{C}_2\text{H}_2)$ normal mode of the η^2 -di σ (CC)- $E(s)$ - $trans$ form computed at 972 cm^{-1} combined with the highly intense $\nu(\text{C}_1-\text{C}_2)$ stretching vibration of the η^2 -di σ (CC)- $E(s)$ - cis complex at 984 cm^{-1} . The presence of a medium peak at 960 cm^{-1} [$\gamma_s(\text{CH})$] for the η^1 -top- $E(s)$ - $trans$ -OSn(1) form augments this signal. In contrast to this intensity increase, the experimental loss peaks at 924, 1029, and at 1646 cm^{-1} become slightly weaker on Pt₂Sn. However, they can again be assigned to the four η^2 -di σ (CC) and η^1 -top-OSn forms.

Besides a large loss signal growing close to the elastic peak at 311 cm^{-1} , two broad and intense bands at 557 and 465 cm^{-1} are recorded in the low-frequency region that can be assigned in an identical manner as on Pt₃Sn(111). The η^2 -di σ (CC)- $E(s)$ - $trans$ complex contributes the intense asymmetric $\nu_{\text{as}}(\text{PtC}_2-\text{PtC}_3)$ vibration computed at 531 cm^{-1} (Pt₃Sn, 524 cm^{-1}) and the $\delta(\text{C}_2=\text{C}_3-\text{C}_4)$ backbone deformation mode at 473 cm^{-1} (Pt₃Sn, 467 cm^{-1}). From the isomeric $E(s)$ - cis complex, again the asymmetric and symmetric $\nu(\text{PtC}_2-\text{PtC}_3)$ molecule-surface stretching vibrations contribute to experimental data. They are calculated at 564 cm^{-1} (Pt₃Sn, 548 cm^{-1}) and at 468 cm^{-1} (452 cm^{-1}), respectively. Again, it becomes obvious that neither the different substrate nor the variation of the coverage influence the frequencies very strongly. In addition,

TABLE 9: Computed Frequencies of Important Normal Modes of Crotonaldehyde Adsorption Structures on $\text{Pt}_2\text{Sn}(111)$, $\Theta = 1/6$ and $1/9$ ML

Pt ₂ Sn(111)						
geometry	η^2 -di σ (CC)-E(s)-trans	η^2 -di σ (CC)-E(s)-cis	η^3 -di σ (CC)- σ (O)-E(s)-cis-OsSn	η^4 - π (CC)-di σ (CO)-E(s)-cis-OsSn	η^1 -top-E(s)-trans-OsSn(1)	η^1 -top-E(s)-trans-OsSn(2)
supercell	3 \times 2	3 \times 2	3 \times 3	3 \times 2	3 \times 3	3 \times 3
ν (C–H) range	3056–2800	3059–2832	3049–2937	3078–2940	3085–2783	3059–2837
ν (C1=O)	1663	1636	1451	1156	1612	1642
ν (C1–C2)	1037	984	1035	982	1150	1177
ν (C2=C3)	1088	1125	1125	1460	1631	1631
ν (C3–C4)	1006	1095	1078	1086	1094	1094
$\nu_{as}(\text{PtC2–PtC3})^a$	531	564	526	511	–	–
$\nu_s(\text{PtC2–PtC3})^a$	326	468	322	396	–	–
$\nu(\text{M–O})^b$	–	–	313	–	103	60
$\nu_{as}(\text{MO–PtCl})^a$	–	–	–	313	–	–
$\nu_{as}(\text{MO–PtCl})^a$	–	–	–	246	–	–

^a These normal modes show complex couplings to other vibrations, which are omitted here for the sake of clarity. ^b This normal mode is only present for η^1 and η^3 forms.

the η^1 -top-OSn forms contribute also with two peaks in that region at 536 and 449 cm^{-1} .

The shoulder measured at 924 cm^{-1} is assigned to the in-phase coupling of the symmetric $\gamma_s(\text{C1H1}-\text{C2H2})$ vibrations with the $\gamma(\text{C3H3})$ mode computed at 938 cm^{-1} . It is increased by the corresponding antiphase linear combination at 907 cm^{-1} . Moreover, both η^1 -top-OSn forms exhibit a peak in that frequency range at 917 and 912 cm^{-1} . At 1090 cm^{-1} , the intense $\nu(\text{C3}-\text{C4})$ stretching vibration of the methyl substituent tilted away from this surface in the η^2 -di $\sigma(\text{CC})$ -*E*-(*s*)-*cis* coordination type, and the $\nu(\text{C2}=\text{C3})$ modes of the isomeric *E*-(*s*)-*trans* form are measured in agreement with the calculated frequencies of 1095 and 1088 cm^{-1} , respectively.

Probably because of their quasi-coplanar orientation, the remaining C—C stretching modes are weak. They are computed at 1037 cm⁻¹ [$\nu(\text{C1}=\text{C2})$] and 1002 cm⁻¹ [$\nu(\text{C3}=\text{C4})$] for the η^2 -di $\sigma(\text{CC})$ -*E*-(*s*)-*trans* form and at 1125 cm⁻¹ [$\nu(\text{C2}=\text{C3})$] and 984 cm⁻¹ [$\nu(\text{C1}=\text{C2})$] for the *E*-(*s*)-*cis* isomer. With the exception of the $\nu(\text{C3}=\text{C4})$ normal mode of the η^2 -*E*-(*s*)-*trans*, which shows significant coupling to deformation modes, the frequencies are perturbed by less than about 15 cm⁻¹ from the values computed for the more stable counterparts on Pt(111).

For the loss peak at 1162 cm^{-1} , a similar interpretation as on the $\text{Pt}_3\text{Sn}(111)$ surface alloy can be developed by taking into account the η^1 -top-OSn structures, which provided loss signals at 1150 and 1176 cm^{-1} . Also the measured loss peaks at 1380 and 1444 cm^{-1} can be assigned with respective vibrations of the η^1 -top-*E*-(*s*)-*trans*-OSn(1) and η^1 -top-*E*-(*s*)-*trans*-OSn(2) structures in the $\delta(\text{CH})$ region (1350 and 1418 cm^{-1} for the first form and 1359 and 1425 cm^{-1} for the second form).

As an intermediate conclusion, the comparison of the vibrational spectra of the η^2 -di σ (CC)-*E*-(*s*)-*trans*, the η^2 -di σ (CC)-*E*-(*s*)-*cis*, and the η^1 -top-*E*-(*s*)-*trans*-OSn forms with the recorded HREELS data still shows a probative agreement.

After annealing the sample further to 200 K, the HREEL spectra (Figure 19) resemble those found for crotonaldehyde on the Pt₃Sn surface alloy at the same temperature. This result is not very surprising because the low-coverage (high temperature) phase on Pt₂Sn(111) corresponds once again to a mixture of the η^2 -di σ (CC)-E(s)-trans, the η^3 -di σ (CC)- σ (O)-E(s)-cis-OSn, and the η^4 - π (CC)-di σ (CO)-E(s)-cis-OSn adsorption forms. Some details on the interpretation of the HREEL spectra at 200 K have already been given in our previous communication,²⁴ so only a brief summary is given here.

Out of the three dominating loss signals at 1090, 1021, and 561 cm^{-1} , the first two bands indicate the presence of the η^2 - $\text{di}\sigma(\text{CC})$ - $E(s)$ - trans [DFT: 1081 cm^{-1} , $\nu(\text{C}2=\text{C}3)$; 1002 cm^{-1} , $\nu(\text{C}3-\text{C}4)$], η^3 - $\text{di}\sigma(\text{CC})$ - $\sigma(\text{O})$ - $E(s)$ - cis -OSn [1016 cm^{-1} , $\gamma''(\text{CH}_3)$], and η^4 - $\pi(\text{CC})$ - $\text{di}\sigma(\text{CO})$ - $E(s)$ - cis -OSn geometry [1015 cm^{-1} , $\gamma''(\text{CH}_3)$], respectively. Less intense, the $\nu(\text{C}2=\text{C}3)$ vibration of the η^3 structure has a calculated value of 1120 cm^{-1} . In agreement with the much weaker π -type interaction mechanism of the $\text{C}2=\text{C}3$ bond with the surface, the corresponding normal mode of the η^4 - $\pi(\text{CC})$ - $\text{di}\sigma(\text{CO})$ - $E(s)$ - cis -OSn form is obtained at 1459 cm^{-1} .

Again, the effect of alloying is more pronounced in the low frequency region, where the $\nu(\text{M}-\text{C})$ and $\nu(\text{M}-\text{O})$ stretching modes and the molecular bending and torsional modes are measured. A narrow, yet intense, band at 561 cm^{-1} is assigned to the asymmetric stretching modes $\nu_{\text{as}}(\text{PtC2}-\text{PtC3})$ of all identified adsorption complexes, which are computed at 525 cm^{-1} for the η^2 and η^3 complexes and at 515 cm^{-1} for the η^4 form.

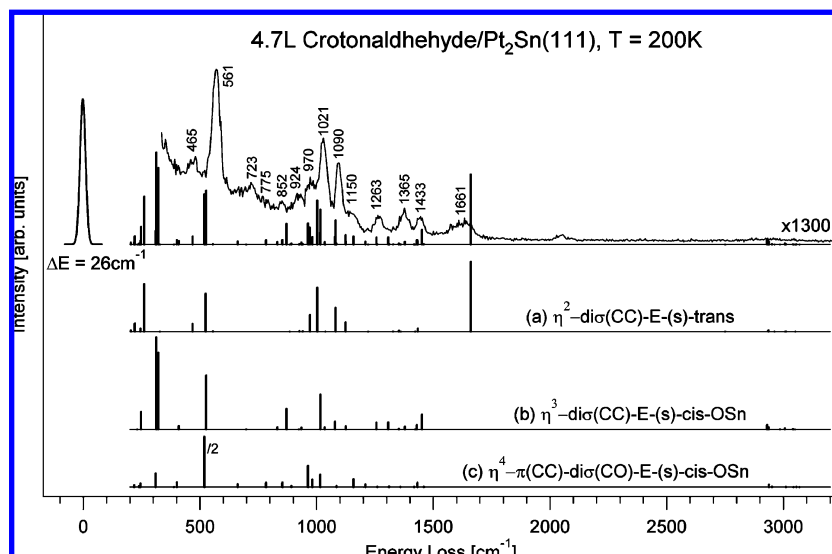


Figure 19. Analysis of the HREELS data of crotonaldehyde (4.7 L) on $(\sqrt{3} \times \sqrt{3})R30^\circ$ -Pt₂Sn/Pt(111) at higher temperatures (200 K) using the computed vibrational spectra of the three competitive η^2 , η^3 , and η^4 structures at low coverage (1/9 ML).

Moreover, around 280 cm^{-1} a highly intense and broad loss signal is measured (FWHM 100 cm^{-1}), which is shifted from the corresponding feature at 259 cm^{-1} on Pt₃Sn. Essentially, all identified adsorption complexes show comparably active normal modes in this region, so the width and intensity of this peak can be rationalized easily. The torsional mode $\tau(\text{C1}-\text{C2})$ of the η^2 form, which gains a large dynamical dipole moment from the lifting of the oxygen, is computed at 261 cm^{-1} . The η^3 structure presents a stronger intensity with the symmetric $\nu_s(\text{PtC2}-\text{C3})$ (DFT, 322 cm^{-1}) and the $\nu(\text{Sn}-\text{O})$ modes (313 cm^{-1}). Finally, the second active molecule–surface stretching mode of the four linear combinations assigned for the η^4 species is calculated at 310 cm^{-1} ; it corresponds to a $\nu_s(\text{PtO}-\text{PtC1})-\nu_s(\text{PtC2}-\text{PtC3})$ normal mode with an antisymmetric lifting of the $\text{O}=\text{C1}$ and the $\text{C2}=\text{C3}-\text{CH}_3$ moieties.

Our results agree well with the combined high-resolution XPS and DFT studies of Göthelid et al.,¹⁶ who proposed the surface species on the Pt₃Sn(111) surface alloy to consist solely of the η^3 -dio(CC)- $\sigma(\text{O})$ -E(s)-cis-OSn and the η^1 -top-E(s)-trans-OSn adsorption complexes. In addition, these authors conclude on the presence of a η^1 -top-E(s)-trans species on Pt₂Sn(111), which is in good agreement with our results.

5. Conclusions

We have successfully employed a combination of HREELS experiments and DFT calculations to investigate the coverage- and temperature-dependent behavior of crotonaldehyde on Pt(111), Pt₃Sn/Pt(111), and Pt₂Sn/Pt(111) and identified the adsorption structures present on these surfaces.

The adsorption structures identified in the phase of irreversibly bonded crotonaldehyde species on Pt(111) at 205 K include a combination of η^2 -dio(CC)-E(s)-trans (−76.0 kJ/mol), η^2 -dio(CC)-E(s)-cis (−73.6), η^3 -dio(CC)- $\sigma(\text{O})$ -E(s)-cis (−76.9), η^4 -dio(CC)-dio(CO)-E(s)-trans (−80.2), and η^4 - $\pi(\text{CC})$ -dio(CO)-E(s)-cis (−68.7) adsorption modes. A variety of other configurations arising from the Z(s)-trans and Z(s)-cis isomers of crotonaldehyde are excluded on the basis of their vibrational fingerprints. They are separated by high rotational energy barriers from the E(s)-trans ground state isomer (12.1 and 15.8 kJ/mol). Compared to the adsorption energies computed for the corresponding configurations of prenal/Pt(111) (−47 to −59 kJ/mol),¹⁵ crotonaldehyde is bonded slightly stronger on Pt(111),

which is a consequence of the substitution effect induced by the second methyl group on the β -carbon.

On the two surface alloys, phase transitions from high coverage at low temperatures to low coverage after annealing are observed, which are characterized by a transformation from vertical adsorptions with low hapticity to more flat structures of higher hapticity. These phase transitions are accompanied by partial desorption processes of intact crotonaldehyde.

At low temperature on Pt₂Sn and Pt₃Sn (155 and 160 K, respectively), a high-coverage-mixed phase of η^2 -dio(CC)-E(s)-trans, η^2 -dio(CC)-E(s)-cis, and η^1 -top-E(s)-trans-OSn structures is detected. Such η^1 -top-OSn forms have also been found previously for prenal on Pt₃Sn/Pt(111) and Pt₂Sn/Pt(111).¹⁵ The low-coverage-mixed phase observed on both surfaces around 200 K is nearly identical and is attributed to the η^2 -dio(CC)-E(s)-trans, η^3 -dio(CC)- $\sigma(\text{O})$ -E(s)-cis-OSn, and η^4 - $\pi(\text{CC})$ -dio(CO)-E(s)-cis-OSn adsorption complexes. On Pt₃Sn the η^2 -dio(CC)-E(s)-cis structure is also present, which is not stable on Pt₂Sn.

The alloying with Sn leads to fewer adsorption modes and to a decrease of the adsorption energies by 40–50% compared to those of pure Pt(111). Although configurations interacting through the Pt–C bonds are weakened, which can be attributed to the electron transfer from Sn to Pt and the downshifts of the d-bands^{23,54} rising with the Sn fraction, the dio(CC) interaction mechanism still leads to competitive η^2 forms. In contrast, the aldehydic function requires an oxygen–tin bond on the surface alloys in order to form stable adsorption structures of η^3 and η^4 hapticities, which require larger ensemble sizes and are only present at low coverages.

The vibrational investigations of the adsorption of crotonaldehyde on the Pt₂Sn(111) surface alloy show an adsorption behavior similar to Pt₃Sn(111). Also, the adsorption energies for the stable structures compare very well on both surface alloys. This is somewhat surprising as a significant decrease of the adsorption strength with rising surface Sn concentration was expected. Importantly, in comparison to Pt(111), neither coverage nor different Sn fractions change the vibrational spectra significantly. The similarity of the vibrational shifts would suggest a rather similar interaction strength on all surfaces in contrast with the expected decrease of the adsorption energies

by alloying. This evident discrepancy will have to be addressed in a more detailed analysis, which we are presently performing.

Acknowledgment. The authors acknowledge the funding by a bilateral CNRS-DFG project. A.K. is grateful to the Alexander von Humboldt and Hertie Foundations for a fellowship. J.H. is grateful for the scholarship grant from the Fonds der Chemischen Industrie.

Supporting Information Available: Crotonaldehyde adsorption energies on Pt(111), Pt₃Sn/Pt(111), and Pt₂Sn/Pt(111) and vibrational assignments of the identified adsorption structures of crotonaldehyde on Pt(111), Pt₃Sn/Pt(111), and Pt₂Sn/Pt(111). This material is available free of charge via the Internet at <http://pubs.acs.org>.

References and Notes

- Jeck, J.; Germain, J. E. *J. Catal.* **1980**, *65*, 133.
- Jerdev, D. I.; Olivas, A.; Koel, B. E. *J. Catal.* **2002**, *205*, 278.
- Surburg, H.; Panten, J. *Common Fragrance and Flavor Materials*; Wiley VCH: New York, 1985.
- Augustine, R. L. *Heterogeneous Catalysis for the Synthetic Chemists*; Marcel Dekker: New York, 1996.
- Bartok, M.; Felföldi, K. *Stereochemistry of Heterogeneous Metal Catalysis*; Wiley: Chichester, U.K.; 1985, Chapter VII.
- Claus, P. *Top. Catal.* **1998**, *5*, 51.
- Gallezot, P.; Richard, D. *Catal. Rev. Sci. Instr.* **1998**, *40*, 81.
- Beccat, J.; Bertolini, J. C.; Gauthier, Y.; Massardier, J.; Ruiz, P. *J. Catal.* **1990**, *126*, 451.
- Birchem, T.; Pradier, C. M.; Berthier, Y.; Cordier, G. *J. Catal.* **1996**, *161*, 68.
- Borgna, A.; Anderson, B. G.; Saib, A. M.; Bluhm, H.; Hävecker, M.; Knop-Gericke, A.; Kuiper, A. E. T.; Tamminga, Y.; Niemantsverdriet, J. W. *J. Phys. Chem. B* **2004**, *108*, 17905.
- Marinelli, T. B. L. W.; Nauburs, S.; Ponc, V. *J. Catal.* **1995**, *151*, 431.
- Marinelli, T. B. L. W.; Ponc, V. *J. Catal.* **1995**, *156*, 51.
- Atrei, A.; Bardi, U.; Wu, J. X.; Zanazzi, E.; Rovida, G. *Surf. Sci.* **1993**, *290*, 286.
- Batzill, M.; Beck, D. E.; Koel, B. E. *Surf. Sci.* **2000**, *466*, L821.
- Haubrich, J.; Loffreda, D.; Delbecq, F.; Sautet, P.; Jugnet, Y.; Bertolini, J. C.; Krupski, A.; Becker, C.; Wandelt, K. *J. Phys. Chem. C* **2008**, *112*, 3701.
- Janin, E.; Schenck, H.; Ringler, S.; Weissenrieder, J.; Åkermark, T.; Göthelid, M. *J. Catal.* **2003**, *215*, 245.
- Overbury, S. H.; Mullins, D. R.; Paffett, M. T.; Koel, B. E. *Surf. Sci.* **1991**, *254*, 45.
- Paffett, M. T.; Gebhard, S. C.; Windham, R. G.; Koel, B. E. *Surf. Sci.* **1989**, *223*, 449.
- Paffett, M. T.; Gebhard, S. C.; Windham, R. G.; Koel, B. E. *J. Phys. Chem.* **1990**, *94*, 6831.
- Paffett, M. T.; Windham, R. G. *Surf. Sci.* **1989**, *208*, 34.
- Zhao, H.; Koel, B. E. *Surf. Sci.* **2004**, *573*, 413.
- Zhao, H.; Koel, B. E. *J. Catal.* **2005**, *234*, 24.
- Delbecq, F.; Sautet, P. *J. Catal.* **2003**, *220*, 115.
- Haubrich, J.; Loffreda, D.; Delbecq, F.; Jugnet, Y.; Sautet, P.; Krupski, A.; Becker, C.; Wandelt, K. *Chem. Phys. Lett.* **2006**, *433*, 188.
- Loffreda, D.; Jugnet, Y.; Delbecq, F.; Bertolini, J. C.; Sautet, P. *J. Phys. Chem. B* **2004**, *108*, 9085.
- de Jesús, J. C.; Zaera, F. *Surf. Sci.* **1999**, *430*, 99.
- Janin, E.; Ringler, S.; Weissenrieder, J.; Åkermark, T.; Karlsson, U. O.; Göthelid, M.; Nordlund, D.; Ogasawara, H. *Surf. Sci.* **2001**, *482*, 83.
- Birchem, T.; Pradier, C. M.; Berthier, Y.; Cordier, G. *J. Catal.* **1994**, *146*, 503.
- Delbecq, F.; Sautet, P. *J. Catal.* **2002**, *211*, 398.
- Delbecq, F.; Sautet, P. *J. Catal.* **1995**, *152*, 217.
- Hirschl, R.; Delbecq, F.; Sautet, P.; Hafner, J. *J. Catal.* **2003**, *217*, 354.
- Loffreda, D.; Delbecq, F.; Vigné, F.; Sautet, P. *J. Am. Chem. Soc.* **2006**, *128*, 1316.
- Eichkorn, K.; Treutler, O.; Öhm, H.; Häser, M.; Ahlrichs, R. *Chem. Phys. Lett.* **1995**, *240*, 283.
- Ahlrichs, R.; Bär, M.; Häser, M.; Horn, H.; Kölmel, C. *Chem. Phys. Lett.* **1989**, *162*, 165.
- Becke, A. D. *Phys. Rev. A* **1988**, *38*, 3098.
- Perdew, J. P. *Phys. Rev. B* **1986**, *33*, 8822.
- Vosko, S. H.; Wilk, L.; Nusair, M. *Can. J. Phys.* **1980**, *58*, 1200.
- Werner, H.-J.; Knowles, P. J.; Amos, R. D.; Bernhardsson, A.; Benning, A.; Celanie, P.; Cooper, D. L.; Deegan, M. J. O.; Dobbyn, A. J.; Eckert, F.; Hampel, C.; Hetzer, G.; Korona, T.; Lindh, R.; Lloyd, A. W.; McNicholas, S. J.; Manby, F. R.; Meyer, W.; Mura, M. E.; Nicklass, A.; Palmieri, P.; Pitzer, R.; Rauhut, R.; Schutz, M.; Stoll, H.; Stone, A. J.; Tarroni, R.; Thosteinsson, T. *MOLPRO 2000*; University College Cardiff Consultants, Ltd.: Wales, U.K., 2000.
- Poirier, R.; Kari, R.; Csizmadia, I. *Handbook of Gaussian Basis Sets*; Elsevier, Amsterdam, 1985; p 225.
- Kresse, G.; Hafner, J. *Phys. Rev. B* **1993**, *47*, 558.
- Kresse, G.; Hafner, J. *Phys. Rev. B* **1993**, *48*, 13115.
- Perdew, J. P.; Wang, Y. *Phys. Rev. B* **1992**, *45*, 13244.
- Kresse, G.; Joubert, D. *Phys. Rev. B* **1999**, *59*, 1758.
- Thakur, S.; Gupta, V. P. *Ind. J. of Pure & App. Phys.* **1998**, *36*, 177.
- Durig, J. R.; Brown, S. C.; Kalasinsky, V. F. *Spectrochim. Acta A* **1976**, *32*, 807.
- de Groot, M. S.; Lamb, J. *Proc. Roy. Soc. (A)* **1957**, *242*, 36.
- Ibach, H.; Mills, D. L. *Electronic Energy Loss Spectroscopy and Surface Vibrations*; Academic Press: New York, 1982.
- Oelichmann, H. J.; Bougeard, D.; Schrader, B. *J. Mol. Struct.* **1981**, *77*, 149.
- Stein, S. E.; Linstrom, P. J.; Mallard, W. G., Eds. *Mass Spectra. In NIST Chemistry WebBook, NIST Standard Reference Database Number 69*; National Institute of Standards and Technology, Gaithersburg MD.
- Redhead, P. A. *Vacuum* **1962**, *12*, 203.
- Steele, W. V.; Chirico, R. D.; Cowell, A. B.; Knipmeyer, S. E.; Nguyen, A. *J. Chem. Eng. Data* **2002**, *47*, 667.
- Becker, C.; Delbecq, F.; Breitbach, J.; Hamm, G.; Franke, D.; Jäger, F.; Wandelt, K. *J. Phys. Chem. B* **2004**, *108*, 18960.
- Delbecq, F.; Vigné-Maeder, F.; Becker, C.; Breitbach, J.; Wandelt, K. *J. Phys. Chem. C* **2008**, *112*, 555.
- Hammer, B.; Nørskov, J. K. *Adv. Catal.* **2000**, *45*, 71.

JP903473M